Computationally Efficient Synchrophasor Estimation: Delayed In-Quadrature Interpolated DFT

César García-Veloso[ID], *Graduate Student Member, IEEE*, Mario Paolone[ID], *Fellow, IEEE*, and José María Maza-Ortega[ID], *Member, IEEE*

Abstract— This article proposes a synchrophasor estimation (SE) algorithm that leverages the use of a delayed in-quadrature complex signal to mitigate the self-interference of the fundamental tone. The estimator, which uses a three-point IpDFT combined with a three-cycle Hanning window, incorporates a new detection mechanism to iteratively estimate and remove the effects caused by interfering tones within the out-of-band interference (OOBI) range. The main feature of the method is its ability to detect interfering tones with an amplitude lower than that adopted by the IEC/IEEE Std. 60255-118, this detection being notably challenging. Furthermore, it simultaneously satisfies all the accuracy requirements for the P and M phasor measurement unit (PMU) performance classes while offering a reduction in the total computational cost compared with other state-of-the-art techniques.

Index Terms— Discrete Fourier transform, IEC/IEEE Std. 60255-118-1-2018, interpolated DFT, phasor measurement unit (PMU), quadrature signal generator, synchrophasor estimation (SE).

I. INTRODUCTION

SINCE their introduction in the 1980s [1], phasor measurement units (PMUs) have evolved and are currently present in the power grids of all developed countries [2] and used successfully in many applications, such as wide-area monitoring protection and control, model validation, and state estimation [3]. To ensure the interoperability and compatibility of PMUs from different manufacturers, an industry standard, whose latest installment corresponds to the IEC/IEEE Std. 60255-118 [4], has been in continuous development since 1992 [5]. The standard [4] defines a set of tests representative of the operating conditions of the power system and the corresponding performance requirements that all PMUs must satisfy based on their class and reporting rate. Two different performance classes are defined in [4]: class P, for applications

requiring a fast response, and class M, for those requiring high accuracy and rejection of interharmonics or subharmonics.

Over the years many synchrophasor estimation (SE) techniques have been explored in the literature, such as wavelets [6], Prony [7], Taylor–Fourier [8], [9], [10], [11], [12], Shanks [13], Kalman filtering [14], [15], [16], subspace-based methods [17], discrete-time frequency-gain transducers [18], complex brick-wall bandpass filters [19], and adaptive filters [20], [21], among others. Most commercial PMUs employ DFT-based SE algorithms [22], which can produce accurate estimates by simply processing a few DFT bins [23]. However, two main limitations compromise the performance of DFT-based techniques: aliasing and spectral leakage [24]. Although the first can be easily solved by increasing the sampling rate or adopting an antialiasing filter, spectral leakage, which includes long- and short-range interferences, requires more elaborate solutions [24]. Long-range leakage refers to the mutual interference caused by all the tones that make up the signal spectrum, while short-range leakage, also known as scalloping or picket fence effect, is the error caused by the displacement of the maximum bin. Long-range leakage can be mitigated by windowing [25], while interpolation of DFT bins [26] addresses short-range leakage. Combining both windowing and interpolation, as proposed in [27], represents the foundation of modern interpolated DFT (IpDFT) techniques. To satisfy the underlying assumption that the signal parameters are fixed within the observation window, and to comply with the time and latency requirements set by [4], intervals of just a few nominal cycles are generally selected [28], [29], [30]. In turn, this causes a coarse frequency resolution which, in the case of a real-valued power system signal whose main tone nominal values fall close to dc, results in the proximity between the positive and negative images. Their mutual interaction, also known as self-interference, constitutes the main source of error in the estimation process [30].

Different approaches have been explored to deal with negative frequency infiltration [23], [28], [29], [30], [31], [32], [33], [34]. Agrež [31] introduced a multipoint weighted IpDFT that reduces the effects of long-range spectral leakage. Belega et al. [23] employed a method based on a novel three-point weighted IpDFT combined with the use of maximum sidelobe decay (MSD) windows, which showed a great rejection of interference from the negative image. Belega and Petri [33]

developed new cosine windows, called maximum image interference rejection with rapid sidelobe decay rate (MIR-RSD) windows, which showed a high rejection of self-interference and long-range leakage from other narrowband disturbances. Romano and Paolone [28] presented an algorithm (e-IpDFT) that iteratively approximated and compensated for the effects of self-interference by taking advantage of the symmetry of the DFT spectrum with respect to the dc component. The method was further extended in [29] to further compensate for an additional generic interfering tone. The resulting method, the so-called i-IpDFT, was proven to meet the requirements for the P and M classes. Both e-IpDFT and i-IpDFT were proved to be computationally efficient and experimentally deployed and validated on industry-grade field-programmable gate arrays (FPGAs) [35], [36]. The same idea of estimating and compensating for the effects of self-interference and long-range leakage from additional tones presented in [29] is also used in [34]. While [29] uses an iterative formulation, [34] derives analytical expressions to achieve faster convergence. However, [34] does not account for subharmonic or interharmonic components.

A different approach to mitigate negative image infiltration is to generate a complex signal from the real one. HT-IpDFT [30] employs a Hilbert filter to approximate the analytic signal and suppress the negative spectrum. Although the method reduces the computational complexity of the iterative process compared with [29], it does not meet the combined requirements of classes P and M for harmonic distortion (HD) (1%) and phase step tests in [4]. Another suitable complex signal to cancel the negative image is the one defined by the signal itself and its imaginary in-quadrature signal. Many quadrature signal generation (QSG) techniques exist and have been used in other applications, such as single-phase phase-locked loops (PLLs) [37]. In [32], an in-quadrature signal is obtained by applying the Clarke transform to a three-phase signal generated by buffering and shifting a noise-filtered version of the measured single-phase signal. The complex signal is further enhanced with a weighted least-squares Taylor–Fourier (WLS-TF) filter to match the magnitudes of both in-quadrature components and is used with a Blackman window filter.

This article proposes an SE algorithm that takes advantage of the use of a delayed in-quadrature complex signal generated in the time domain to mitigate the self-interference of the fundamental tone. A delayed in-quadrature formulation is adopted due to its simplicity, low computational cost, and, as will be shown, excellent performance. The estimator, named time-delay IpDFT (TD-IpDFT), uses a three-point IpDFT combined with a Hanning window and incorporates a new detection mechanism to iteratively estimate and remove the effects caused by interfering tones equal to or greater than 4% within the out-of-band interference (OOBI) range. It simultaneously satisfies all accuracy requirements for the P and M classes, while offering a reduction in the total computational cost compared with the i-IpDFT [29], [36].

Although a single PMU capable of meeting the requirements of both classes at once is advantageous, to the best of our knowledge, very few works in the literature can achieve this. Belega et al. [11], Duda and Zielinski [18], Razo-Hernandez et al. [19], and Roscoe et al. [20] present

techniques that can be used to comply with the P or M classes, but not both simultaneously. Roscoe [21] improves the work of [20] and proposes a hybrid P- and M-class PMUs that relies on a tunable trigger threshold used to detect transients and, accordingly, selects between two parallel P-class and M-class algorithms. In [10], a transient detector is also employed to select between two sets of output obtained, respectively, with two Taylor–Fourier algorithms of different lengths and window parameters. The resulting PMU is designed to meet the requirements of both classes at once, while each individual algorithm is not intended to individually meet the requirements of the P or M classes. Similarly, [30] also relies on a transient event detection mechanism to select between the output of two parallel Hilbert filters of different orders. In addition to [29], [17] also proposes a single algorithm to simultaneously meet the requirements of both classes. The method, named harmonic-mean-estimation of signal parameters via rotational invariance techniques (HM-ESPRIT), enhances subspace-based PMU estimation methods, by considering an HM to dynamically estimate the size of the signal subspace while reducing the computational burden of ESPRIT [38]. It manages to comply with all tests, except the step tests, where its maximum overshoot exceeds the P class requirements.

In view of the earlier, the main contributions of this article are as follows.

1) A novel SE IpDFT-based method that simultaneously satisfies all accuracy requirements for the P and M classes.
2) The use of a delayed in-quadrature complex signal generated in the time domain to mitigate the self-interference of the fundamental tone and reduce the total computational cost compared with the i-IpDFT.
3) A new detection mechanism to iteratively estimate and remove the effects caused by interfering tones equal to or greater than 4% within the OOBI range.

This article is structured as follows. Section II reviews the fundamentals of IpDFT-based SE techniques. Section III describes the theoretical basis of how a complex signal consisting of in-quadrature components allows the suppression of the negative image spectrum. Section IV presents the structure, formulation, and adjustment of the parameters of the TD-IpDFT SE algorithm. Section V presents the complete characterization of the algorithm for P- and M-class PMUs indicated by [4] drawing a side-by-side comparison with the i-IpDFT. Section VI presents the experimental setup and tests used for the validation of the theoretical findings of Section V. Section VII discusses and compares the performance of the TD-IpDFT with other state-of-the-art SE methods. Finally, VIII summarizes the main findings and gives closing remarks.

II. SE IpDFT TECHNIQUES: FUNDAMENTALS

We refer to a formulation that considers a Hanning window function, which offers a good compromise between sidelobe decay and mainlobe width [27], and a three-point DFT interpolation scheme, as it reduces the effects of long-range leakage [31]. This configuration, already adopted in [29] and [30], is also used for the proposed TD-IpDFT.

A. Three-Point (3p) IpDFT Based on the Hanning Window

Consider a discrete single-tone steady-state signal $x(n)$

$$x(n) = A_0 \cos(2\pi f_0 n T_s + \varphi_0), \quad n \in \mathbb{Z} \tag{1}$$

where T_s represents the sampling period and A_0, f_0, and φ_0 are the fundamental amplitude, frequency, and initial phase, respectively. If a window of N consecutive samples starting at $n = 0$ is selected, the DFT spectrum of the signal $X(k)$ is given by (2), where $w(n)$ is the discrete windowing function and $B = \sum_{n=0}^{N-1} w(n)$ the DFT normalization factor

$$X(k) = \frac{1}{B} \sum_{n=0}^{N-1} w(n) x(n) e^{-j2\pi kn/N}, \quad k \in [0, N-1]. \tag{2}$$

According to the convolution theorem, a conjugate spectrum is obtained, where each spectral component $X(k)$ is the result of the combined contributions of a positive and negative image of the fundamental tone, each being the scaled and rotated versions of the DFT of the window function $W(k)$ shifted at $\pm f_0/\Delta_f$[1]

$$X(k) = \underbrace{V_0 W(k - f_0/\Delta_f)}_{\text{Positive Image}} + \underbrace{V_0^* W(k + f_0/\Delta_f)}_{\text{Negative Image}} \tag{3}$$

where $V_0 = A_0 e^{j\varphi_0}$. The distance between positive and negative images depends on the frequency resolution Δ_f, which is the reciprocal of the length of the selected window $T = N T_s$. For the Hanning window, $W(k)$ corresponds to

$$W_H(k) = 0.5 W_R(k) - 0.25(W_R(k-1) + W_R(k+1)) \tag{4}$$

where $W_R(k)$ is the DFT of the rectangular window, also known as the Dirichlet kernel

$$W_R(k) = e^{-j\pi k(N-1)/N} \frac{\sin(\pi k)}{\sin(\pi k/N)}, \quad k \in [0, N-1]. \tag{5}$$

Given a set of estimates of the signal parameters $(\hat{f}, \hat{A}, \hat{\varphi})$ and knowing the windowing function adopted, the spectral contributions of positive and negative images can be estimated by

$$\hat{X}_{H\pm}(k) = \hat{A} e^{\pm j\hat{\varphi}} W_H(k \mp \hat{f}/\Delta_f). \tag{6}$$

For the general case of incoherent sampling,[2] the fundamental tone of the signal falls between subsequent bins. Thus, the signal frequency (SF) can be expressed as

$$f_0 = (k_m + \delta)\Delta_f, \quad \delta \in [-0.5, 0.5) \tag{7}$$

where k_m is the index of the highest bin and δ a fractional correction term that, for the Hanning window (δ_H), can be analytically calculated by interpolating the three highest DFT bins as [31]

$$\delta_H = 2\varepsilon \frac{|X_H(k_m + \varepsilon)| - |X_H(k_m - \varepsilon)|}{|X_H(k_m - \varepsilon)| + 2|X_H(k_m)| + |X_H(k_m + \varepsilon)|} \tag{8}$$

where $\varepsilon = \pm 1$ if $|X_H(k_m + 1)| \gtrless |X_H(k_m - 1)|$.

[1]In the case of a real multitone signal, its spectrum will be result of the combined contributions from the positive and negative images of each individual tone.

[2]Incoherent sampling refers to the adoption of a window length (T) which does not contain an integer number of fundamental periods ($1/f_0$), i.e., $\delta \neq 0$.

With δ_H determined, the amplitude and phase of the fundamental tone are given by

$$A_{0_H} = 2|X_H(k_m)| \left| \frac{\pi \delta_H}{\sin(\pi \delta_H)} \right| |\delta_H^2 - 1| \tag{9a}$$

$$\varphi_{0_H} = \angle X_H(k_m) - \pi \delta_H. \tag{9b}$$

III. NEGATIVE FUNDAMENTAL IMAGE SUPPRESSION

A. Delayed In-Quadrature Technique

Consider a complex discrete single-tone steady-state signal $\bar{y}(n)$, with components $y(n)$ and $y(n - d_\theta)$, θ being the resulting phase shift that delay d_θ ($d_\theta \in \mathbb{N}$) introduces at the corresponding frequency f_0

$$\bar{y}(n) = \underbrace{A_0 \cos(\omega_0 n T_s)}_{y(n)} + j \underbrace{A_0 \cos(\omega_0 n T_s - \theta)}_{y(n-d_\theta)}, \quad n \in \mathbb{N} \tag{10}$$

where $\omega_0 = 2\pi f_0$ is the angular frequency[3] and $\theta = \omega_0 d_\theta T_s$. If (10) is expressed in terms of complex exponentials and the positive and negative frequency components are grouped, the following expression is obtained:

$$\bar{y}(n) = \underbrace{\frac{1}{2} A_0 e^{j(\omega_0 n T_s)} \sigma_+}_{\text{Positive Frequency}} + \underbrace{\frac{1}{2} A_0 e^{-j(\omega_0 n T_s)} \sigma_-}_{\text{Negative Frequency}}, \quad n \in \mathbb{N} \tag{11}$$

where σ_+ and σ_- are the complex positive and negative delay gains and correspond to

$$\sigma_+ = 1 + e^{j(\pi/2 - \theta)} \tag{12a}$$

$$\sigma_- = 1 + e^{j(\pi/2 + \theta)}. \tag{12b}$$

The complex signal $\bar{y}(n)$ can be seen as a "filtered" version of $y(n)$, where the amplitude and phase of each positive and negative frequency component are altered, respectively, by (12a) and (12b) based on the relative angular shift θ. Let $\lfloor \ldots \rceil$ be the round-to-the-nearest integer function, rounding the equidistant values away from zero to the integer with a larger magnitude. Fig. 1 shows the frequency response of a "filtered" delayed in-quadrature complex signal $\bar{y}(n)$ generated considering a frequency f from a signal $y(n)$ with normalized frequency $f_0[\text{pu}] = f_0/f$. The magnitude and phase response for each positive and negative frequency component are given, respectively, by $|\sigma_+|$, $\angle \sigma_+$ and $|\sigma_-|$, $\angle \sigma_-$ with $d_\theta = \lfloor f_s/(4f) \rceil$. The frequency response is 4-pu periodic and is centered on the frequency considered for in-quadrature generation f (1 pu). If there is no discrepancy between the SF (f_0) and that used for the generation of the in-quadrature component, i.e., ($f_0 = f \rightarrow f_0[\text{pu}] = 1$), a perfect in-quadrature signal is obtained, resulting in cancellation of the negative image ($\sigma_- = 0$) and doubling of the positive one ($\sigma_+ = 2$). Otherwise, if the SF falls in its vicinity ($f_0 \simeq f \rightarrow f_0[\text{pu}] \simeq 1$), still a significant mitigation of the negative image occurs, but the effects can only be quantified by (12) once the SF has been estimated.

[3]Although for simplicity the initial angle has been set to 0, the same result holds if considered.
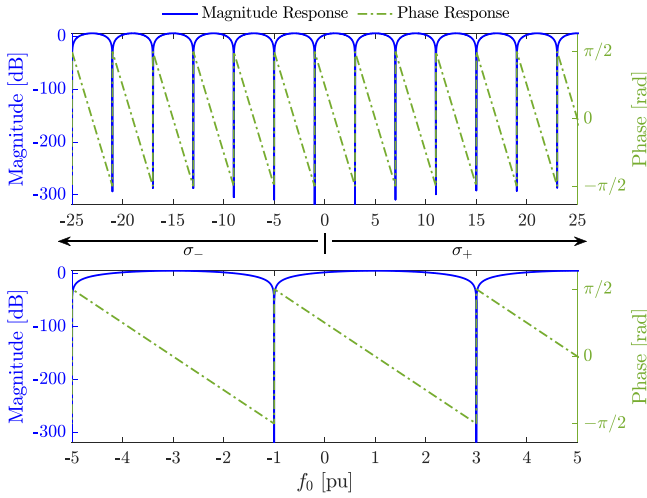
Fig. 1. Frequency response of a "filtered" delayed in-quadrature complex signal $\bar{y}(n)$ generated considering a frequency f from a signal $y(n)$ with normalized frequency $f_0[pu] = f_0/f$. Wide view (top) and zoomed-in view (bottom).

Algorithm 1 TD-QSG Algorithm

Input: $[x(n)]$
1: $d_0 = \left\lfloor \frac{f_s}{4 f_n} \right\rceil$
2: $\bar{x}_o(n) = x(n) + j x(n - d_0)$
3: $X_o(k) = \mathtt{DFT}[\bar{x}_o(n)]$
4: $X_{o_H}(k) = 0.5 X_o(k) - 0.25(X_o(k-1) + X_o(k+1))$
5: $\{\hat{f}_0\} = \mathtt{IpDFT}[X_{o_H}(k)]$
6: $d_f = \left\lfloor \frac{f_s}{4 \hat{f}_0} \right\rceil$
7: $\bar{x}_f(n) = x(n) + j x(n - d_f)$
Output: $\{\bar{x}_f(n)\}$

B. Adopted Delayed Structure

A delayed in-quadrature complex signal generation technique is adopted. Conceptually, an in-quadrature component, given a sampled single-tone steady-state signal $(x(n))$ as defined in (1), can be generated by delaying it by $\lfloor f_s/(4 f_0) \rceil$. Since f_0 is not known in advance, a two-step delayed in-quadrature complex signal generation method based on the IpDFT, the so-called time-delay QSG (TD-QSG), is proposed. The method is described in Algorithm 1, where the functions $\mathtt{DFT}$ and $\mathtt{IpDFT}$ refer, respectively, to (2) and (7)–(9).

First, an initial approximation of the in-quadrature complex signal $(\bar{x}_o(n))$ is generated delaying the sampled signal $(x(n))$ by d_0 samples. These correspond to the rounded delay given by the nominal frequency f_n (lines 1 and 2). The spectrum of the complex signal is then calculated and windowed in the frequency domain considering a three-cycle Hanning window[4] (lines 3 and 4). A three-point IpDFT is then applied to just obtain a refined estimate of the SF $(\hat{f}_0)$ (line 5), which is subsequently used to obtain a refined delay d_f and in-quadrature complex signal $(\bar{x}_f(n))$ (lines 6 and 7).

---

[4]This has been found to be the shortest window length required to detect and remove all tones defined by the OOBI test.

IV. TD-IpDFT TECHNIQUE

This section describes the TD-IpDFT algorithm by providing: 1) a presentation of its underlying signal model (Section IV-A); 2) a description of its structure and formulation (Section IV-B); 3) a novel trigger mechanism for OOBI identification and removal; 4) a sensitivity analysis to choose its most suitable parameters (Section IV-C); and 5) an analysis of its computational complexity (Section IV-D). The proposed method is an improvement over the i-IpDFT proposed in [29] and [36] and its aim is to match the performance of the i-IpDFT while presenting a lower computational cost by using a delayed in-quadrature complex signal to mitigate the effects of self-interference.

A. Signal Model

The same static signal model within the analysis window $(n \in [0, N-1])$ used in [29] and [36] is considered by the TD-IpDFT so that $x(n)$ is the result of a fundamental tone and a potential single interference tone with amplitudes, frequencies and initial phases, respectively, denoted by $A_0, A_i, f_0, f_i, \varphi_0$ and φ_i

$$x(n) = \underbrace{A_0 \cos(\omega_0 n T_s + \varphi_0)}_{\text{Fundamental Tone}} + \underbrace{A_i \cos(\omega_i n T_s + \varphi_i)}_{\text{Interference Tone}} \quad (13)$$

where $\omega_0 = 2\pi f_0$ and $\omega_i = 2\pi f_i$ denote the angular frequencies of the fundamental and interference tones. By operating with $x(n)$, the TD-IpDFT estimates the fundamental tone's parameters $\{\hat{A}_0, \hat{f}_0, \hat{\varphi}_0\}$ as well as those of an additional interference tone $\{\hat{A}_i, \hat{f}_i, \hat{\varphi}_i\}$ if detected.

B. Structure and Formulation

The TD-IpDFT algorithm incorporating the OOBI compensation routine is summarized using the diagram in Fig. 2 and the pseudocode in Algorithm 2, where the functions $\mathtt{TD\text{-}QSG}$, $\mathtt{TD\text{-}SR}$, $\mathtt{TD\text{-}APc}$, and $\mathtt{wf}$ refer, respectively, to Algorithms 1, 3, and 4 and (4)–(6), while Fig. 3 shows the spectra at different steps of the process. First, the delayed in-quadrature complex signal $(\bar{x}_f)$ is generated using Algorithm 1 (line 1), followed by the calculation of its DFT spectrum and the application of the Hanning window in the frequency domain (lines 2 and 3). The IpDFT is then applied to obtain a first estimate of the signal parameters (line 4). Subsequently, an interference compensation loop is initiated (line 6) after the initialization of some auxiliary variables (line 5). These include the initial estimates of the positive $(\hat{X}_{i+}^0)$ and negative $(\hat{X}_{i-}^0)$ spectrums of a potential interference tone, the previous normalized energy of the residual spectrum (R_e^0), along with the residual energy exit (τ_{R_e}) and interference (τ_i) trigger flags.

Within the loop, provided that the residual energy exit flag has not been triggered in the previous iteration, the contribution of the fundamental tone is first estimated $(\hat{X}_0^{q-1})$ by
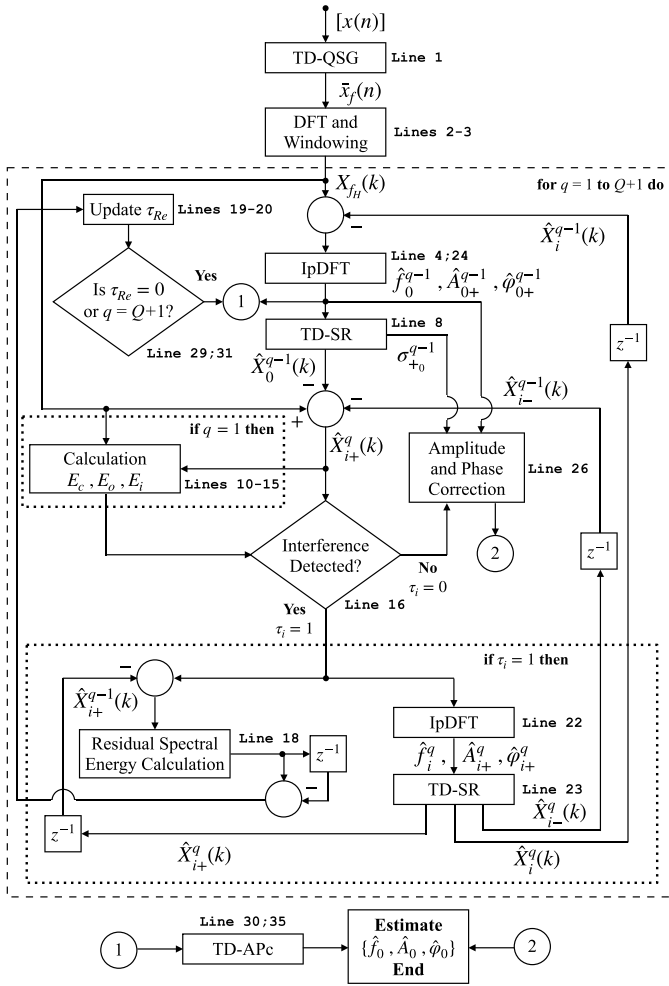
Fig. 2. Diagram of the TD-IpDFT Algorithm. The process is looped $Q + 1$ times instead of Q as in the pseudocode in Algorithm 2 since the IpDFT function on line 4 is nested within the loop. The correspondence between the main blocks and the lines in Algorithm 2 is reported side to each block.

means of Algorithm 3[5] (line 8). Together with the previously estimated negative spectrum of the interference tone ($\hat{X}_{i-}^{q-1}$), $\hat{X}_0^{q-1}$ is removed from the original spectrum (line 9) and used to determine whether such narrowband components may be present. The analysis of such bins, which should correspond to a positive image of a spurious tone, is performed during the first iteration (lines 10–15). Among them, only those where an interference tone is expected are considered, i.e., for a nominal three-cycle window $k \in [0-2] \cup [4-7]$.[6] Once the highest magnitude bin k_c has been determined (14), its total energy and that of its two closest neighbors are aggregated into E_c (15) (line 11). The calculated E_c is then compared with

---

[5] Algorithm 3, named time-delay spectral reconstruction (TD-SR), calculates the spectrum of any tone "α" in a delayed in-quadrature complex signal ($\bar{x}_f$) given estimates of its frequency ($\hat{f}_\alpha$) and those of the uncorrected amplitude ($\hat{A}_{\alpha+}$) and phase ($\hat{\varphi}_{\alpha+}$) of its positive image. This is done by calculating the positive ($\sigma_{+\alpha}$) and negative ($\sigma_{-\alpha}$) complex delay gains (Algorithm 3: lines 1 and 2), which can then be used to obtain the spectral contributions of both positive and negative images (Algorithm 3: lines 3–6).

[6] For $T = 3/f_n$, bins $[0-2] \cup [4-7]$ correspond to a frequency range $[0-2]\Delta_f \cup [4-7]\Delta_f$ Hz, where $\Delta_f = 1/T$. This is where most of the energy of a potential OOBI is located.

Algorithm 2 TD-IpDFT Algorithm

Input: $[x(n)]$
1: $\{\bar{x}_f(n)\} = \text{TD-QSG}[x(n)]$
2: $X_f(k) = \text{DFT}[\bar{x}_f(n)]$
3: $X_{f_H}(k) = 0.5X_f(k) - 0.25(X_f(k-1) + X_f(k+1))$
4: $\{\hat{f}_0^0, \hat{A}_{0+}^0, \hat{\varphi}_{0+}^0\} = \text{IpDFT}[X_{f_H}(k)]$
5: $\hat{X}_{i+}^0(k) = 0; \hat{X}_{i-}^0(k) = 0; R_e^0 = 0; \tau_{R_e} = 1; \tau_i = 0$
6: **for** $q = 1$ **to** Q **do**
7:   **if** $\tau_{R_e} = 1$ **then**
8:     $\{\hat{X}_0^{q-1}(k), \sigma_{+0}^{q-1}\} = \text{TD-SR}[\hat{f}_0^{q-1}, \hat{A}_{0+}^{q-1}, \hat{\varphi}_{0+}^{q-1}]$
9:     $\hat{X}_{i+}^q(k) = X_{f_H}(k) - \hat{X}_0^{q-1}(k) - \hat{X}_{i-}^{q-1}(k)$
10:     **if** $q = 1$ **then**
11:       Apply (14)-(15)-(16)
12:       **if** $(\frac{E_c}{E_o} \in [\lambda_o^l, \lambda_o^u]$ **and** $\frac{E_c}{E_i} \geq \lambda_i)$ **or** $\frac{E_c}{E_o} > \lambda_o^u$ **then**
13:         $\tau_i = 1$
14:       **end if**
15:     **end if**
16:     **if** $\tau_i = 1$ **then**
17:       $\hat{X}_r^q(k) = \hat{X}_{i+}^q(k) - \hat{X}_{i+}^{q-1}(k)$
18:       $R_e^q = \sum |\hat{X}_r^q(k)|^2/E_o$
19:       **if** $|R_e^q - R_e^{q-1}| < \lambda_{R_e}$ **then**
20:         $\tau_{R_e} = 0$
21:       **end if**
22:       $\{\hat{f}_i^q, \hat{A}_{i+}^q, \hat{\varphi}_{i+}^q\} = \text{IpDFT}[\hat{X}_{i+}^q(k)]$
23:       $\{\hat{X}_i^q(k), -, \hat{X}_{i+}^q(k), \hat{X}_{i-}^q(k)\} =$
      $\text{TD-SR}[\hat{f}_i^q, \hat{A}_{i+}^q, \hat{\varphi}_{i+}^q]$
24:       $\{\hat{f}_0^q, \hat{A}_{0+}^q, \hat{\varphi}_{0+}^q\} = \text{IpDFT}[X_{f_H}(k) - \hat{X}_i^q(k)]$
25:     **else**
26:       $\hat{\varphi}_0^q = \hat{\varphi}_{0+}^q - \angle\sigma_{+0}^q; \hat{A}_0^q = \frac{\hat{A}_{0+}^q}{|\sigma_{+0}^q|}$
27:       **break**
28:     **end if**
29:   **else**
30:     $\{\hat{A}_0^q, \hat{\varphi}_0^q\} = \text{TD-APc}[\hat{f}_0^q, \hat{A}_{0+}^q, \hat{\varphi}_{0+}^q]$
31:     **break**
32:   **end if**
33: **end for**
34: **if** $q = Q$ **then**
35:   $\{\hat{A}_0^Q, \hat{\varphi}_0^Q\} = \text{TD-APc}[\hat{f}_0^Q, \hat{A}_{0+}^Q, \hat{\varphi}_{0+}^Q]$
36: **end if**
Output: $\{\hat{f}_0, \hat{A}_0, \hat{\varphi}_0\}$

Algorithm 3 TD-SR Algorithm

Input: $[\hat{f}_\alpha, \hat{A}_{\alpha+}, \hat{\varphi}_{\alpha+}]$
1: $\varphi_{d_\alpha} = 2\pi \hat{f}_\alpha d_f T_s$
2: $\sigma_{+\alpha} = 1 + e^{j(\frac{\pi}{2}-\varphi_{d_\alpha})}; \sigma_{-\alpha} = 1 + e^{j(\frac{\pi}{2}+\varphi_{d_\alpha})}$
3: $\hat{\varphi}_{\alpha-} = -(\hat{\varphi}_{\alpha+} - \angle\sigma_{+\alpha}) + \angle\sigma_{-\alpha}$
4: $\hat{A}_{\alpha-} = \hat{A}_{\alpha+}\frac{|\sigma_{-\alpha}|}{|\sigma_{+\alpha}|}$
5: $\hat{X}_{\alpha+}(k) = \text{wf}[\hat{f}_\alpha, \hat{A}_{\alpha+}, \hat{\varphi}_{\alpha+}]; \hat{X}_{\alpha-}(k) = \text{wf}[-\hat{f}_\alpha, \hat{A}_{\alpha-}, \hat{\varphi}_{\alpha-}]$
6: $\hat{X}_\alpha(k) = \hat{X}_{\alpha+}(k) + \hat{X}_{\alpha-}(k)$
Output: $\{\hat{X}_\alpha(k), \sigma_{+\alpha}, \hat{X}_{\alpha+}(k), \hat{X}_{\alpha-}(k)\}$

---

three heuristically defined threshold levels (λ_o^l, λ_o^u, and λ_i), which allow for the identification of a potential interference
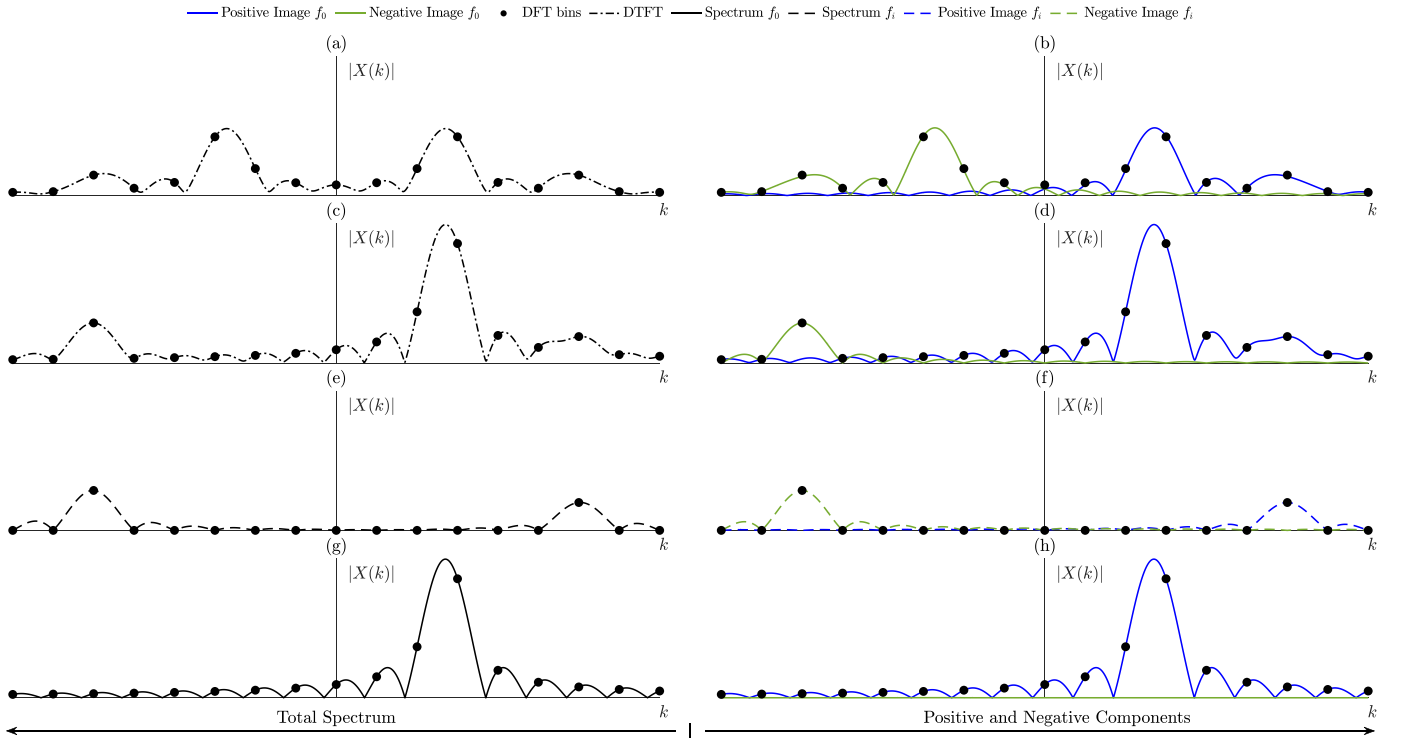
Fig. 3. Spectra at different steps of Algorithm 2 for a discrete signal $x(n)$ affected by additive white Gaussian noise with a signal-to-noise ratio (SNR) equal to 80 dB [$x(n) = A_0 \cos(2\pi f_0 n T_s) + A_i \cos(2\pi f_i n T_s)$, $n \in \mathbb{Z}$; where $A_0 = 1$, $f_0 = 45$ Hz, $A_i = 0.35$ and $f_i = 100$ Hz]. (a) and (b) $X_{0_H}(k)$ in line 1 (line 4 of Algorithm 1). (c) and (d) $X_{f_H}(k)$ in line 3. (e) $X_{f_H}(k) - \hat{X}_0^{q-1}(k)$ within line 9. (f) $\hat{X}_i^q(k)$ in line 23. (g) $X_{f_H}(k) - \hat{X}_i^{q-1}(k)$ within line 24. (h) $\hat{X}_0^{q-1}(k)$ in line 8 (subsequent iteration). The rectangular window is used to represent all spectra, so the effects of long-range spectral leakage are noticeable. Similarly, a 35% HD is selected for the same reason.

(lines 12–14) (see Section IV-C). These thresholds measure the relation of E_c to the total original spectral energy E_o (16a) (λ_o^l, λ_o^u) and to the entire set of interference bins E_i (16b) (λ_i), that is, $\forall k \in [0, K-1]$.

$$k_c = \arg\max_k |\hat{X}_{i+}(k)|; \quad k \in [0, 2] \cup [4, 7] \qquad (14)$$

$$E_c = \sum_k |\hat{X}_{i+}(k)|^2; \quad \begin{cases} k \in [0, 2], & \text{if } k_c = 0 \\ k \in [5, 7], & \text{if } k_c = 7 \\ k \in [k_c \pm 1], & \text{otherwise} \end{cases} \qquad (15)$$

For efficient implementation, a routine stop criterion is introduced inspired by the one proposed in [30], where the incremental ratio between consecutive values of E_i/E_o was evaluated. Instead, the evolution of the total normalized residual spectral energy R_e is used. This is defined as the total remaining energy after subtracting both the estimated fundamental and the interfering tones inferred by the previous iteration from the original spectrum (17) normalized by the total original spectral energy E_o. If the variation falls below a predefined threshold level (λ_{R_e}), τ_{R_e} is set to zero to stop the iterative process (see Section IV-C) (lines 17–21).

$$E_o = \sum_{k=0}^{K-1} |X_{f_H}(k)|^2 \qquad (16a)$$

$$E_i = \sum_{k=0}^{K-1} |\hat{X}_{i+}(k)|^2 \qquad (16b)$$

$$R_e^q = \sum_{k=0}^{K-1} |X_{f_H}(k) - \hat{X}_0^{q-1}(k) - \hat{X}_i^{q-1}(k)|^2 / E_o \qquad (17)$$

The second IpDFT is then applied to estimate the parameters of the positive image of the interfering component (line 22), which are used to approximate the complete spectrum of the interfering tone ($\hat{X}_i^q(k)$) (line 23). Finally, the last IpDFT can be applied to $X_{f_H}(k) - \hat{X}_i^q(k)$, obtaining an improved estimate of the fundamental $\{\hat{f}_0^q, \hat{A}_{0+}^q, \hat{\varphi}_{0+}^q\}$ (line 24). The process is looped Q times or until τ_{R_e} is triggered. The final results, the initial estimates, if no interferences are found, or the latest, once τ_{R_e} is triggered or the maximum number of iterations is reached ($q = Q$), are then corrected to account for the amplitude and phase alterations due to the use of the delayed in-quadrature complex signal ($\bar{x}_f$). If no interferences are found, the amplitude and phase corrections can be applied directly (line 26), since the fundamental positive complex delay gain (σ_{+0}^{q-1}) is already obtained when Algorithm 3 is applied to estimate the fundamental spectrum (line 8). Otherwise, this is done using Algorithm 4[7] (lines 30 and 35). Finally, fundamental frequency estimations at two successive reporting times (m and $m-1$) are used to calculate the rate-of-change-of-frequency (ROCOF) at the reporting time m with a

---

[7]Algorithm 4, named time-delay amplitude and phase correction (TD-APc), corrects the estimated amplitude and phase of the positive image of any tone "α" in $\bar{x}_f$ given $\hat{f}_\alpha$, $\hat{A}_{\alpha+}$, and $\hat{\varphi}_{\alpha+}$.

Algorithm 4 TD-APc Algorithm

Input: $[\hat{f}_\alpha, \hat{A}_{\alpha+}, \hat{\varphi}_{\alpha+}]$
1: $\varphi_{d_\alpha} = 2\pi \hat{f}_\alpha d_f T_s$; $\sigma_{+_\alpha} = 1 + e^{j(\frac{\pi}{2} - \varphi_{d_\alpha})}$;
2: $\hat{\varphi}_\alpha = \hat{\varphi}_{\alpha+} - \angle\sigma_{+_\alpha}$; $\hat{A}_\alpha = \dfrac{\hat{A}_{\alpha+}}{|\sigma_{+_\alpha}|}$

Output: $\{\hat{A}_\alpha, \hat{\varphi}_\alpha\}$

---

first-order backward approximation of a first-order derivative

$$\hat{\dot{f}}_0(m) = \left(\hat{f}_0(m) - \hat{f}_0(m-1)\right) F_r \tag{18}$$

where F_r denotes the reporting rate.

C. Novel Trigger Mechanism for OOBI Compensation

A novel trigger mechanism for the OOBI that builds on and expands the normalized spectral energy method proposed in [29] is adopted. In [29], an energy threshold capable of identifying interfering components with distortion equal to or greater than 10% was adjusted based on a characterization of the energy content shown by each test condition specified in [4]. A first refinement is proposed on the basis of an improved selection of the DFT bins to calculate the spectral energy. Although all bins in the interference spectrum were considered in [29], only k_c, and its two closest neighbors, are now selected. The ratio between E_c and E_o is called *spectral energy ratio*. As shown in [29], the amplitude and phase steps are the main limiting signal dynamics when setting an adequate energy threshold. However, their energy is spread across the whole spectrum, whereas, in the case of an interfering tone, it will be concentrated around its frequency. This is leveraged by introducing an additional metric to enhance the distinction between interfering tones and other spurious contributions of different origins. The so-called *spectral energy concentration ratio* allows us to measure the spread of spectral energy around k_c by taking the relation between E_c and E_i.

Setting appropriate values for λ_o^l, λ_o^u and λ_i allows for the identification and correction of OOBIs below the limit of 10% set by [4]. To account for more realistic conditions and derive more robust thresholds, multidynamic signals, beyond the scope of [4], have been simulated. Fig. 4 shows the variability of E_c/E_o and E_c/E_i using a boxplot representation for each test condition in [4]. All regular tests in [4] have been combined with an amplitude modulation (AM) (except for the AM itself and the OOBI) and evaluated for an SNR equal to 60 and 80 dB. In addition, each test is executed 20 times considering different initial phase angles for the generation of the reference signal equally distributed between 0 and 2π. This is done to modify the relative positions of the successive analysis windows throughout the test duration. AMs were selected because they present the second highest energy content, just after the steps. For each test, a 10% AM with the highest modulating frequency within the range [0.1–5] Hz, so that the resulting estimates are compliant with [4], has been used.[8] All test signals combined with an AM are marked

with *. Disregarding the amplitude modulated steps (PS* and AS*), Fig. 4 (top) reveals how a minimum of 4% OOBI can be distinguished from the other signal types by selecting a $\lambda_o^l = 4.9 \cdot 10^{-4}$. Lower levels of OOBI fall within the phase and amplitude modulated range (PM*). Additionally, the 10% amplitude modulated harmonic distortion (HD 10%*) also exhibits some outliers that exceed this limit. These correspond to the second harmonic, which can also be corrected with the iterative process since [4] also requires taking it into consideration as part of the frequency range under analysis within the OOBI test. For the magnitudes considered in [4], the remaining harmonics do not impact the estimation of the fundamental due to the sidelobe attenuation offered by the Hanning window.[9] Furthermore, setting $\lambda_o^u = 2.4 \cdot 10^{-3}$ allows distinguishing OOBIs with an amplitude greater than or equal to 9% from amplitude-modulated steps (PS* and AS*).

Regarding the value of λ_i, only an examination of the operating conditions that fall within the band defined by both λ_o^u and λ_o^l is necessary. Namely, the amplitude-modulated steps. Therefore, a value of 0.765 has been chosen, which allows us to account for the *spectral energy concentration ratio* of all OOBI distortion levels from 4% to 9%. Both OOBI cases are plotted (while the latter represents the most critical case) since the ratio decreases as the distortion level increases. A small overlap can still be seen in Fig. 4 (bottom) regarding the PS* as well as some outliers for the AS*. However, the
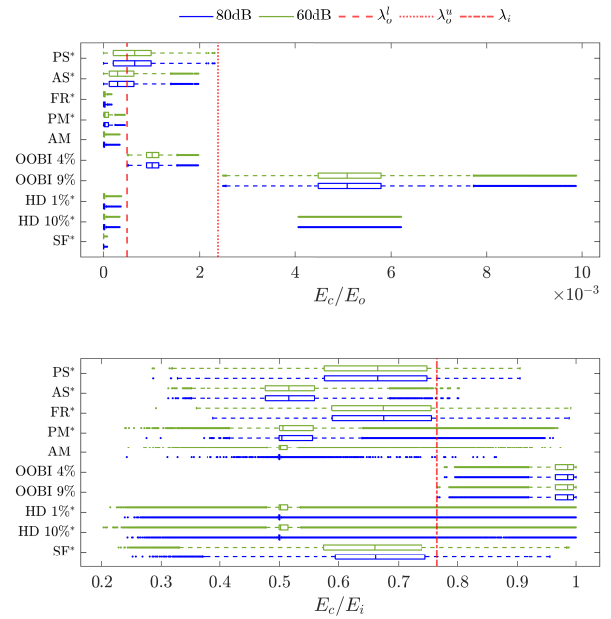

Fig. 4. Boxplot representation of E_c/E_o (top) and E_c/E_i (bottom). All operating conditions marked with * present a 10% AM with the highest modulating frequency within the range of [0.1–5] Hz compliant with [4]. The compliance is verified for all tests with 80-dB noise in terms of TVE, FE, and RFE, and for the step tests according to their response times (R_t).

---

[8]The compliance is verified for all tests with 80-dB noise in terms of total vector error (TVE), frequency error (FE), ROCOF error (RFE), and for the step tests according to their response times (R_t).

[9]It is important to remark that this attenuation also allows the TD-IpDFT to maintain the same level of accuracy for those cases where a fundamental tone is simultaneously corrupted by a single OOBI interference and any combination of HD, excluding the second harmonic, for the harmonic magnitude levels considered in [4]. However, the same cannot be guaranteed when there are multiple simultaneous interferences within the OOBI range given the signal model adopted (Section IV-A).
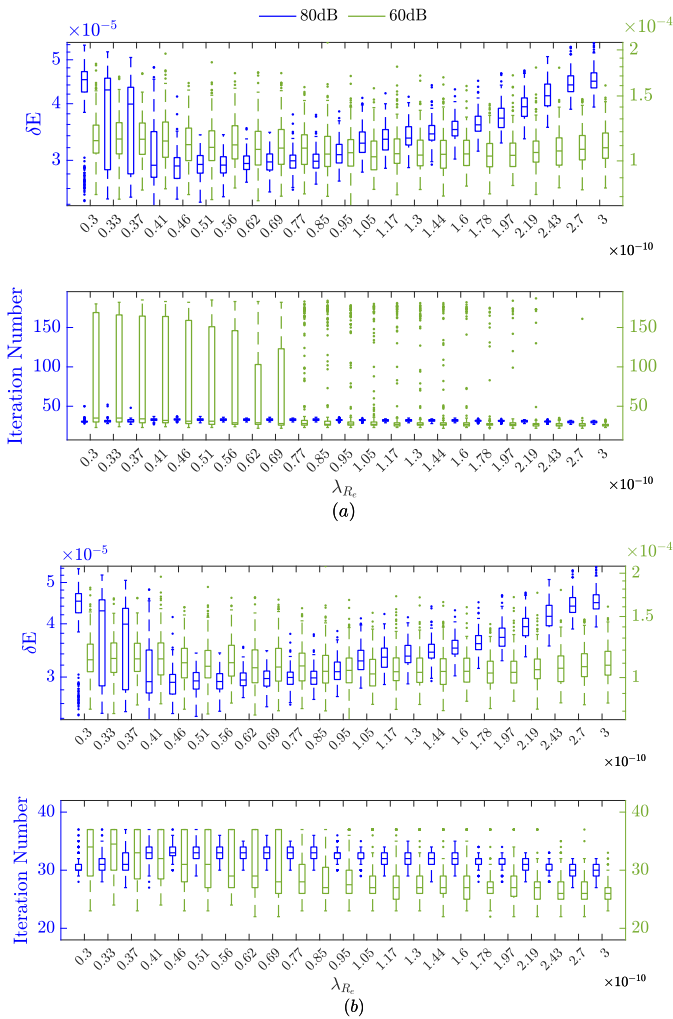
Fig. 5. Boxplot representation of the error in estimating the correction term δ (8) (top) and the total number of iterations (bottom) for different values of λ_{R_e}. The maximum number of iterations Q is set to (a) 200 and (b) 37.

simulation results according to the standard [4] did not show any impact on their respective tests. All the cases (top and bottom) reveal that noise levels have no significant impact on the magnitude of neither E_c/E_o nor E_c/E_i. Only for the latter in the AM tests can the effects of noise be noticed significantly.

Finally, the adjustment of λ_{R_e} described in Section IV-B is analyzed. This is done by simulating 200 consecutive runs of a 10% distortion OOBI test for 23 different potential threshold values. These have been selected within the $3 \cdot 10^{-10}$ to $3 \cdot 10^{-11}$ range based on a previous coarse estimation. Each run consists of 97 windows of analysis for each interfering tone $f_i \in [10–25] \cup [75–100]$ Hz and considers three fundamental frequency f_0 values of 47.5, 50, and 52.5 Hz. The analysis is done by accounting for SNRs equal to 60 and 80 dB and allowing the iterative process to run, if unstopped, for a sizeable number of iterations. Additionally, between runs, the initial phase angle used to generate the reference test signal has been shifted by $2\pi/64$ to further account for the relative positions of the analysis windows. Fig. 5 shows the variability of the error in estimating the correction term δ (8) and in the total number of iterations executed for a maximum Q equal to 200 [Fig. 5(a)] and 37 [Fig. 5(b)]. The error estimates of δ

(δE) consider the maximum global error among all simulated interfering tones

$$\delta E = \max_{f_i} \left(\max_{f_0} (\delta E_{f_0 f_i}) \right) \tag{19}$$

where $\delta E_{f_0 f_i}$ is the error in estimating the correction term δ (8) given a signal characterized by a fundamental frequency f_0 and a 10% interference signal f_i. Despite a noticeable performance trend in δE for the 80 dB case, a more uniform behavior is shown for a 60-dB noise. As shown in Fig. 5(a), for the 60-dB case, although no single run reached the maximum iteration limit (Q) of 200, all considered threshold values λ_{R_e}, with the exception of $\lambda_{R_e} = 2.43 \cdot 10^{-10}$ and $\lambda_{R_e} = 3 \cdot 10^{-10}$, presented runs where a large number of executed iterations were required. Although the adoption of $\lambda_{R_e} = 2.43 \cdot 10^{-10}$ or $\lambda_{R_e} = 3 \cdot 10^{-10}$ would limit computational cost by reducing the maximum number of required iterations, it would also compromise accuracy, as both values result in a significantly higher δE at a lower noise level. Fig. 5(b) examines the impact of limiting the maximum number of iterations (Q) to 37 on δE.[10] The results show that there are no significant changes in the error values obtained compared with Fig. 5(a). Thus, a $\lambda_{R_e} = 6.9 \cdot 10^{-11}$ is selected as a tradeoff between accuracy and computational performance. This value ensures the lowest maximum δE ($1.678 \cdot 10^{-4}$) for the higher noise case (60 dB) when considering a maximum $Q = 36$ while almost matching the same error level as the lowest δE for 80 dB.

D. Computational Complexity

To evaluate the feasibility of the TD-IpDFT to be implemented in an embedded device and compare its performance with other state-of-the-art techniques, its computational complexity is here analyzed. Table I summarizes the total number of arithmetic operations required by the TD-IpDFT [both in the event an interference tone is detected "TD-IpDFT (OOBI)" or not "TD-IpDFT (no int.)"] as well as those used by its constituent functions, e.g., IpDFT. As in [29] and [30], the difference between simple operations $(+ \quad - \quad \times)$, complex operations $(\div \ \sin \ \angle \ |\ldots| \ \lfloor\ldots\rceil \ \arg\max)$, and function calls (such as calls to predefined subroutines or algorithms, e.g., IpDFT) is drawn. Likewise, the total cost is expressed in terms of the total number of DFT bins calculated, K, and the maximum number of executions of the iterative process Q. The results show a total of 640 simple operations and 176 complex operations are required if no interference is detected, and $171 + 1000Q$ simple and $37 + 307Q$ complex operations considering the OOBI iterative compensation for eight DFT bins. For a maximum 36 iterations the total number of operations results in 36 171 simple and 11 089 complex operations. No explicit method had been specified so far for the calculation of the DFT bins or for generating the delayed in-quadrature complex signal ($\bar{x}_f(n)$). As indicated in [29], if a small number of DFT bins are needed, recursive computation methods are generally more efficient. Among them, the mSDFT technique [39] is guaranteed to be stable without sacrificing accuracy

[10]A value of $Q = 37$ has been selected as it corresponds to the maximum number of iterations required to attain the lowest maximum δE within the 80-dB case in Fig. 5(a).

TABLE I
TD-IpDFT COMPUTATIONAL COMPLEXITY

	Simple Operations			Complex Operations						Func. Calls
Constituent Func.	$+$	$-$	$\times$	$\div$	sin	$\angle$	$\|...\|$	$\lfloor...\rceil$	arg max	$g(h)$
(h_1) IpDFT (3p)	3	4	8	2	1	1	4	-	-	-
(h_2) wf	$3K+1$	$4K+3$	$17K+11$	$K+2$	$6K+8$	-	-	-	-	-
(h_3) TD-QSG[a]	$3K+3$	$3K+2$	$4K+7$	2	-	-	3	2	-	-
(h_4) TD-SR	$2K+4$	4	6	1	4	2	2	-	-	$2(h_2)$
(h_5) TD-APc	1	2	5	1	2	1	1	-	-	-
	Simple Operations			Complex Operations						Func. Calls
Total Algorithm 2[a]	$+$	$-$	$\times$	$\div$	sin	$\angle$	$\|...\|$	$\lfloor...\rceil$	arg max	$g(h)$
TD-IpDFT (no int.)	$3K-1$	$5K+7$	$2K+3$	1	-	1	$2K+1$	-	1	$\sum_i^{1,3,4}(h_i)$
TD-IpDFT (OOBI)	$3K-1+$ $Q(K-1)$	$K+6+$ $Q(8K+2)$	$2K+3+$ $Q(K+1)$	-	-	-	$2K+$ $Q(K+1)$	-	1	$(h_3)+(h_5)+$ $2Q(h_4)+$ $(2Q+1)(h_1)$

[a] For comparison with other existing methods we have included the operations to obtain the delayed in-quadrature complex spectrum from the buffered windowed DFT bins of the real signal, as shown in Fig. 6.
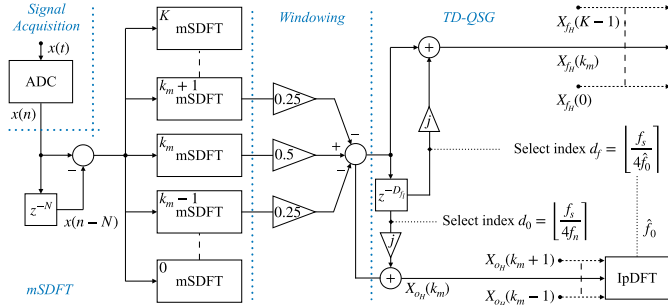
Fig. 6. Combined mSDFT and TD-QSG implementation.

and has been used by previous implementations of IpDFT algorithms in embedded FPGA-based PMU devices [35], [36]. Consequently, Fig. 6 presents the proposed implementation to obtain the windowed delayed in-quadrature complex signal spectrum. For efficiency, as suggested in [39], a common buffer is used for all mSDFT modules. Moreover, the delayed in-quadrature complex spectrum is obtained by buffering the windowed DFT bins of the real signal $X_{o_H}(k)$. As indicated in Algorithm 1 the method relies on an IpDFT to refine the final delay based on an initial nominal quadrature, and thus, select the appropriate past DFT bins from the buffer D_{f_l}. The size of the DFT buffer D_{f_l} depends on the lowest expected SF, sampling rate, and the required number of DFT bins K. For a minimum frequency of 45 Hz, 50 kHz sampling rate, and eight bins, its minimum theoretical size will be roughly $1.5\times$ that of the one required by the mSDFT.

V. PERFORMANCE ASSESSMENT

In this section, a complete evaluation of the TD-IpDFT algorithm is performed by comparing its performance with the static and dynamic accuracy limits indicated in [4] for the performance classes P and M, as well as by means of a side-by-side comparison with the i-IpDFT [29], [36]. The assessment is carried out in a MATLAB simulation environment in terms of TVE, FE, RFE, and response (R_t)

and delay times (D_t) for the step tests. As in [29] and [30], a nominal frequency of 50 Hz and a reporting rate of 50 frames per second (fps) were selected to limit the number of tests. Each test is performed using a three-nominal cycle window and considering two levels of additive white Gaussian noise (AWGN). Noise levels with SNRs equal to 60 and 80 dB have been selected, as previously used in [29] and [30], as they allow to consider the uncertainty of the measurement and simulate more realistic conditions. All test signals are synthesized by superimposing on the noise-free reference signal indicated in [4] an AWGN whose variance (σ_n^2) is calculated according to

$$\sigma_n^2 = \left(\frac{A_0/\sqrt{2}}{10^{\text{SNR}/20}} \right)^2 \qquad (20)$$

where A_0 is the fundamental amplitude of the noise-free reference signal and SNR is the noise level in dB. All simulations are carried out according to the parameters given in Table II, which have been selected to ensure a fair comparison between both methods. The justification for the selection of Q for the i-IpDFT is provided in Section VII. All results are presented by means of stacked graphs that summarize the resulting performance against the maximum permissible limits set by [4] (Figs. 7–10). Finally, the maximum values resulting from each test case are reported together again with the accuracy limits indicated in [4] in Tables III–V. Both Figs. 7–9 and Tables III and IV also include the results of the experimental validation tests for better clarity and ease of comparison (see Section VI for details of the experimental setup and validation tests).

A. Static Tests

Three static tests are defined in [4] to evaluate the performance of the algorithm under steady-state conditions: the SF range test, the HD test, and the OOBI test. For all tests, a simulation time of 1 s has been considered and consecutive analysis windows based on the selected PMU reporting rate

TABLE II
TD-IpDFT AND i-IpDFT PARAMETERS

Parameter	Variable	Value	
		TD-IpDFT	i-IpDFT
Nominal System Frequency	f_n	50 Hz	50 Hz
Window Type	-	Hann	Hann
Window Length	T	60 ms $\left(\frac{3}{f_n}\right)$	60 ms $\left(\frac{3}{f_n}\right)$
Sampling Rate	f_s	50 kHz	50 kHz
PMU Reporting Rate	F_r	50 fps	50 fps
DFT bins	K	8	8
Max Number of Iterations	Q	36	44
IpDFT Interpolation Points	-	3	3
Lower Spectr. Energy Thr.	λ_o^l	$4.9 \cdot 10^{-4}$	-
Upper Spectr. Energy Thr.	λ_o^u	$2.4 \cdot 10^{-3}$	-
Spectr. Energy Conc. Thr.	λ_i	0.765	-
Res. Energy Variation Thr.	λ_{R_e}	$6.9 \cdot 10^{-11}$	-
OOBI Detection Threshold	λ	-	$3.3 \cdot 10^{-3}$
Self-Inter. comp. (fund)	P_0	-	1
Self-Inter. comp. (inter)	P_i	-	2

Fig. 8. OOBI Results. (a) OOBI test ($A_{ih} = 10\%A_0$; single interference) [4]. (b) Maximum error per OOBI interference level.

Fig. 7. Static tests. (a) SF range test. (b) HD test ($A_h = 10\%A_0$; single harmonic) [4].

Fig. 9. Dynamic tests. (a) AM test (depth 10%). (b) PM test (depth $\pi/18$ rad). (c) FR test [4].

(F_r) are evaluated. Each test is repeated a total of 256 times to modify the relative position of the different observation windows. This is done using different initial phase angles equally distributed between 0 and 2π for the generation of the reference signal. The worst case results among all windows are then considered. The results of all static tests are presented in Figs. 7 and 8 and Table III.

The results of the SF range test [Fig. 7(a)] show how the accuracy of the method does not depend on the fundamental tone frequency but rather on the total noise level, resulting in errors of one higher order of magnitude for the lower SNR. As reported in Table III, maximum TVE values of 0.030% (60 dB) and 0.003% (80 dB) are obtained, well below the required 1% limit. Likewise, similar trends also apply for the FE and RFE maximum errors, where respective values of 1.48 mHz (60 dB) and 0.16 mHz (80 dB) for the frequency and 0.013 Hz/s (80 dB) for the ROCOF are obtained, in accordance with the limit requirements of 5 mHz and 0.1 Hz/s. For the
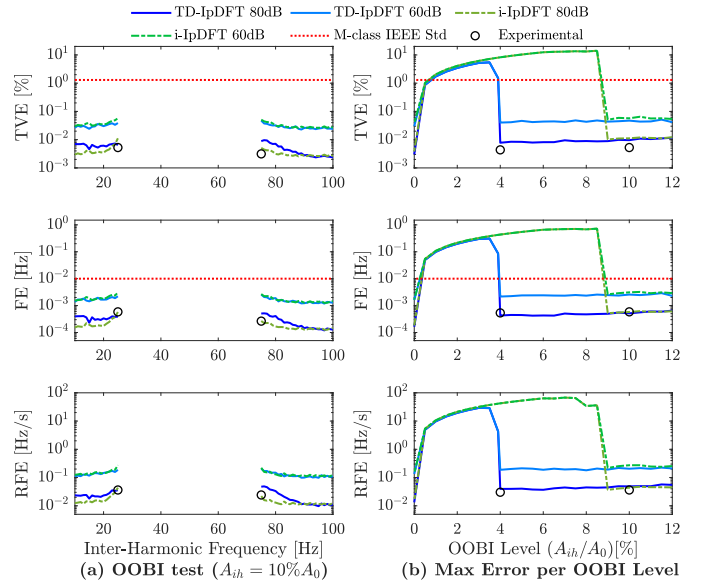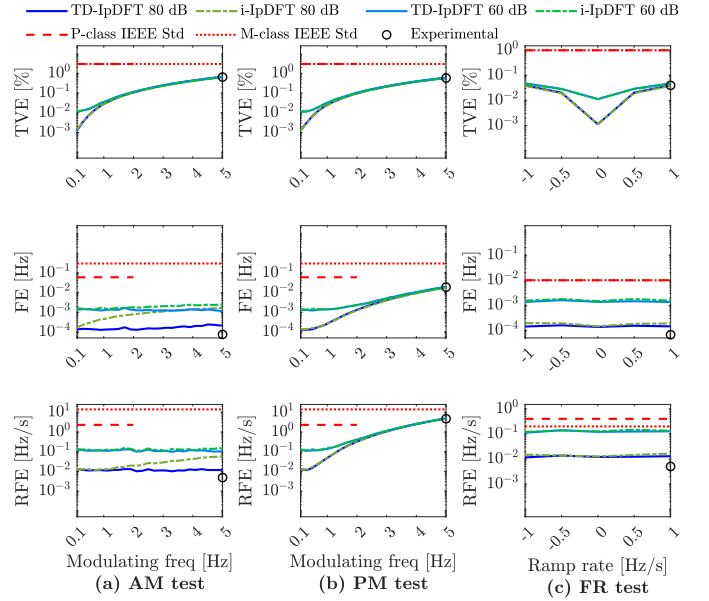
higher noise case, a ROCOF value of 0.128 Hz/s is obtained, which is above the M class limit. The same trend can be seen in Fig. 7(a) for the different fundamental frequency values. This is explained because, as was also the case in [29] and [30], under the higher noise conditions, spurious RFE values can marginally exceed the most stringent limit of class M. Given that only the worst case results are reported and the substantial amount of analysis windows considered, as a result of both the duration of each test and the number of tests conducted, these values simply reflect those captured spurious violations of the M class limit.

The results of the HD test are shown in Fig. 7(b) for a total HD (THD) of 10% and in Table III for both THDs of 1% and 10%. Again, no significant performance difference

TABLE III

MAXIMUM TVE, FE, AND RFE IN STATIC TESTS AND MAXIMUM LIMIT ALLOWED BY [4]

	TVE[%]						FE[mHz]						RFE[Hz/s]					
	Std P / M	Hann $(3/f_n)$					Std P / M	Hann $(3/f_n)$					Std P / M	Hann $(3/f_n)$				
		TD-IpDFT			i-IpDFT			TD-IpDFT			i-IpDFT			TD-IpDFT			i-IpDFT	
SNR [dB]		60	80	Ex	60	80		60	80	Ex	60	80		60	80	Ex	60	80
SF	1 / 1	0.030	0.003	0.001	0.033	0.004	5 / 5	1.48	0.16	0.07	1.68	0.19	0.4 / 0.1	0.128	0.013	0.006	0.145	0.017
HD 1%	1 / 1	0.028	0.003	-	0.032	0.003	5 / 25	1.48	0.15	-	1.55	0.16	0.4 / -	0.127	0.013	-	0.126	0.013
HD 10%	1 / 1	0.027	0.003	0.001	0.031	0.003	5 / 25	1.50	0.15	0.06	1.43	0.14	0.4 / -	0.116	0.012	0.005	0.127	0.013
OOBI 10% f_l[b]	- / 1.3	0.039	0.009	0.005	0.057	0.011	- / 10	2.22	0.51	0.59	3.11	0.58	- / -	0.187	0.047	0.036	0.273	0.044
OOBI 10% f_n	- / 1.3	0.034	0.006	-	0.044	0.004	- / 10	2.10	0.38	-	2.12	0.21	- / -	0.157	0.032	-	0.178	0.018
OOBI 10% f_u[b]	- / 1.3	0.047	0.010	0.003	0.051	0.005	- / 10	2.57	0.52	0.26	2.68	0.27	- / -	0.205	0.049	0.024	0.222	0.022
OOBI 4%[a] f_l[b]	- / 1.3	0.040	0.008	0.004	8.245	8.227	- / 10	2.09	0.43	0.54	436	436	- / -	0.188	0.040	0.030	42.43	42.37
OOBI 4%[a] f_n	- / 1.3	0.037	0.006	-	7.440	7.427	- / 10	1.88	0.34	-	393	392	- / -	0.158	0.030	-	38.71	38.65
OOBI 4%[a] f_u[b]	- / 1.3	0.039	0.007	0.002	8.209	8.195	- / 10	2.17	0.43	0.33	434	434	- / -	0.167	0.033	0.019	42.24	42.17

[a] Maximum limit values taken from [4] for the 10% case.

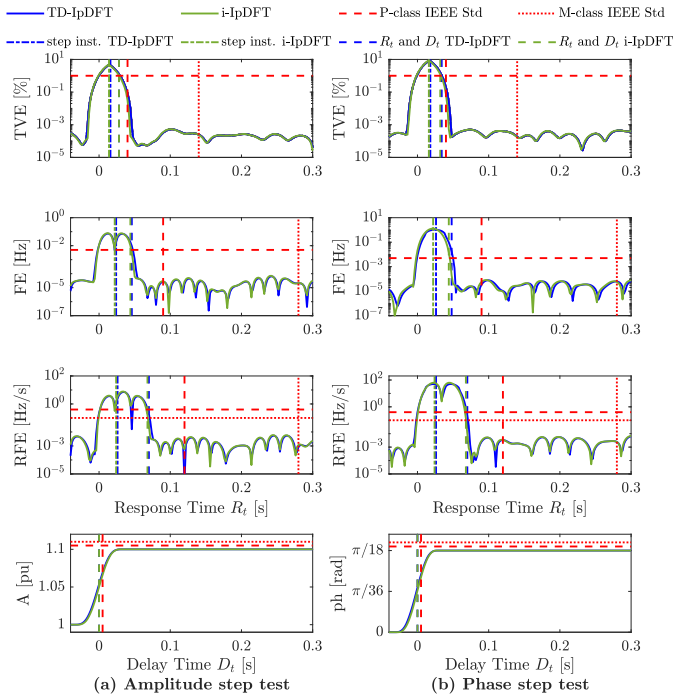[b] $f_l = f_n - 0.1F_r/2$; $f_u = f_n + 0.1F_r/2$.

Fig. 10.   Step tests. (a) Amplitude step test (+10%). (b) Phase step test (+π/18) [4].

closer the interference is to the fundamental tone, the more difficult it is to detect and remove it. This trend is evident in Fig. 8(a) for the lower noise level, as the maximum registered values increase as they approach the fundamental tone frequency. These maximum values, together with those for a 4% distortion, disaggregated by each fundamental frequency, are presented in Table III. For the TD-IpDFT, all values are well within the performance requirements of class M. It is important to note that no performance requirement is provided in [4] for interfering signals with a magnitude other than 10% of the fundamental. Thus, the same reference values have been considered for the 4% case. As shown, the newly proposed trigger mechanism for OOBI is capable of correcting interferences with amplitudes equal to or greater than 4%, showing a very similar performance to the 10% case. This represents an improvement over the detection mechanism used in [29] and [30], which was only able to detect and correct interferences equal to or greater than 10%. In the presence of an interfering tone with an amplitude of less than 4%, the same level of accuracy cannot be guaranteed as the iterative process is not activated. This is illustrated in Fig. 8(b), where the performance of the new mechanism is shown by means of the maximum values of TVE, FE, and RFE registered among all interfering tones and fundamental frequency values for different OOBI interference levels.

B. Dynamic Tests

Two dynamic tests are defined in [4] to evaluate the performance of the algorithm under time-varying conditions: the measurement bandwidth test and the frequency ramp (FR) test. For all bandwidth tests, a $\lceil 2/f_m \rceil$ s simulation time has been considered, while the FR tests use a $12/|R_f|$ s instead (where f_m and R_f denote, respectively, the modulating frequency and the ramp rate).[11] In both cases, consecutive analysis windows based on the selected F_r are evaluated, with each test repeated 256 times to modify the relative positions of the observation

is detected on the basis of the order of the interference tone, but rather on the total noise level. The 1% performance limit is far from the maximum TVE values reported for the 60 dB case of 0.028% (1% THD) and 0.027% (10% THD) in Table III. Specifically, the maximum values of FE and RFE were 1.48 mHz (1% THD) and 1.50 mHz (10% THD) for the frequency and 0.127 Hz/s (1% THD) and 0.116 Hz/s (10% THD) for the ROCOF. All are within the most demanding 5 mHz and 0.4 Hz/s limit requirements for devices of class P.

Finally, regarding the OOBI test, Fig. 8(a) shows the maximum value of TVE, FE, and RFE obtained for each interference tone among the three simulated fundamental frequency values of 47.5, 50, and 52.5 Hz considering a total interharmonic distortion of 10% as required by [4]. The

[11]All FR tests consider two $1/|R_f|$ s presteady-state and poststeady-state periods before and after the FR. For the particular case of $R_f = 0$, a simple 12-s steady-state case is analyzed.

TABLE IV

MAXIMUM TVE, FE, AND RFE IN DYNAMIC TESTS AND MAXIMUM LIMIT ALLOWED BY [4]

	TVE[%]					FE[mHz]					RFE[Hz/s]				
	Std	Hann $(3/f_n)$					Std	Hann $(3/f_n)$					Std	Hann $(3/f_n)$			
	P / M	TD-IpDFT			i-IpDFT		P / M	TD-IpDFT			i-IpDFT		P / M	TD-IpDFT		i-IpDFT	
SNR [dB]		60	80	Ex	60	80		60	80	Ex	60	80		60	80	Ex	60	80
AM	3 / 3	0.653	0.647	0.64	0.612	0.608	60 / 300	1.67	0.24	0.08	2.46	1.66	2.3 / 14	0.132	0.013	0.005	0.154	0.060
PM	3 / 3	0.590	0.584	0.58	0.553	0.547	60 / 300	19.93	19.03	19.00	18.63	17.72	2.3 / 14	4.813	4.735	4.744	4.716	4.644
FR	1 / 1	0.048	0.040	0.04	0.046	0.038	10 / 10	1.60	0.16	0.07	1.78	0.19	0.4 / 0.2	0.141	0.014	0.005	0.147	0.017

TABLE V

MAXIMUM RESPONSE, DELAY TIMES, AND OVERSHOOTS IN STEP TESTS AND LIMITS ALLOWED BY [4]

	TVE Response Time [ms]					FE Response Time [ms]					RFE Response Time [ms][a]				
	Std	Hann $(3/f_n)$					Std	Hann $(3/f_n)$					Std	Hann $(3/f_n)$		
	P / M	TD-IpDFT		i-IpDFT		P / M	TD-IpDFT		i-IpDFT		P / M	TD-IpDFT		i-IpDFT	
SNR [dB]		60	80	60	80		60	80	60	80		60	80	60	80
AS	40 / 140	28	28	28	28	90 / 280	48	48	46	46	120 / 280	108	72	108	68
PS	40 / 140	36	36	34	34	90 / 280	54	54	50	48	120 / 280	110	74	110	72

	Delay Time [ms]					Max Overshoot [%]				
	Std	Hann $(3/f_n)$				Std	Hann $(3/f_n)$			
	P / M	TD-IpDFT		i-IpDFT		P / M	TD-IpDFT		i-IpDFT	
SNR [dB]		60	80	60	80		60	80	60	80
AS	5 / 5	2	2	2	2	5 / 10	0.099	0.010	0.101	0.010
PS	5 / 5	2	2	2	2	5 / 10	0.068	0.007	0.068	0.007

[a] The RFE response times have been calculated considering all crossings with the M class accuracy band limit of 0.1 Hz/s within a 148 ms window around the step. This is done to exclude spurious RFE values that marginally exceed said limit under the higher SNR of 60 dB solely due to noise.

windows. This is done using different initial phase angles equally spaced between 0 and 2π for the generation of the reference signal. Finally, the worst case results among all evaluated windows are considered. The results of all dynamic tests are presented in Fig. 9 and Table IV.

The most demanding requirements set by [4] correspond to class P, with TVE, FE, and RFE values, respectively, of 3%, 60 mHz, and 2.3 Hz/s for both AM and phase modulation (PM). In the case of FRs, class M sets the most stringent limits with TVE, FE, and RFE thresholds of 1%, 10 mHz, and 0.2 Hz/s, respectively. As shown in Fig. 9(a) and (b), both measurement bandwidth tests show how the algorithm exhibits similar TVEs. The total error increases with the modulation frequency and becomes the predominant source of error, masking the effect of noise for modulating frequencies above 1 Hz. However, the trends for the FE and RFE differ. On the one hand, in the PM test [Fig. 9(b)], the TD-IpDFT method reveals a pattern like the one of the TVE, where higher modulating frequencies result in higher errors and noise as the main source of error is overridden. However, in the AM test [Fig. 9(a)], the algorithm can provide accurate frequency and ROCOF estimates without being affected by the modulation frequency. It is worth noting how for the lower noise the TD-IpDFT outperforms the i-IpDFT in terms of FE and RFE for the AM test, as shown in Fig. 9(a), where the FE and RFE of the latter increase with the modulating frequency f_m. All maximum errors fall well within the limits set in [4]. The worst case results of the FR test are shown in Fig. 9(c) for ramps with different positive and negative rates. Maximum

values are presented in Table IV. The TD-IpDFT is shown to provide accurate frequency and ROCOF estimates, in line with those of the SF test and unaffected by the ramp rate, and maximum TVEs of 0.048% (60 dB) and 0.040% (80 dB), which depend on the magnitude of the ramp rate but not on its sign, fully meeting performance requirements.

C. Step Tests

Instantaneous changes in the amplitude (AS) ($\pm 10\%$) or phase (PS) ($\pm \pi/18$) of the signal are defined in [4] to evaluate the performance of the algorithm in a transient event. All step tests are conducted considering a simulation time of 1 s, with the step occurring at 0.5 s. For a more rigorous analysis, 400 different initial phase angles for the generation of the reference signal have been considered to account for different relative step positions on top of 50 consecutive runs for each noise level. This analysis is conducted for both positive and negative tests. The results of both steps are shown in Fig. 10(a) and (b) for a single-noise run and an initial signal phase equal to 0, and the worst case response, delay times, and maximum overshoot values across all initial signal phases and noise runs evaluated are presented in Table V. All results correspond to the positive step cases (similar results are obtained in the case of a negative step) and are only plotted for the 80-dB case for better clarity. Both Fig. 10(a) and (b) represents TVE, FE, and RFE as a function of their respective response times, which means that each time axis is centered at the moment when the accuracy limit is first exceeded.
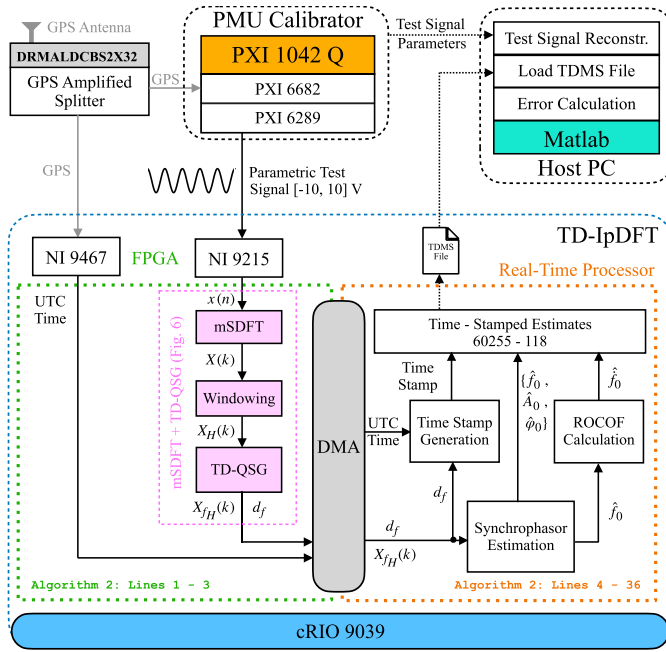
Fig. 11.   Overview of the experimental setup used for validation.

Likewise, the estimated phase and amplitude are shown as functions of their respective delay time, with their time axis centered at the instant each step occurs. The results show how the proposed algorithm meets all the requirements, with all estimates within the limits. It is important to note that no significant impact is found by the noise level during the transient, besides the presteady-state and poststeady-state accuracy already shown by the static tests.

VI. Experimental Validation

A. Experimental Setup

An overview of the experimental setup used for the validation is shown in Fig. 11. The two key components are the PMU calibrator and the CompactRIO-9039.

1) *PMU Calibrator:* The PMU calibrator, fully characterized in [40], is here operated in an open-loop configuration. Its PXI-1042Q chassis from National Instruments (NI), Austin, TX, USA [41], powered by an NI PXI-8110 controller, has a NI PXI-6682 GPS module and a NI PXI-6289 board for data acquisition and transmission. As shown in [40], the device is capable of generating reference synchrophasors characterized by uncertainties of 0.00x% and 0.0x% on their TVEs, respectively, for static and dynamic conditions. The calibrator is used to synthesize user-defined parametric waveforms, replicating the test conditions imposed by the IEC/IEEE Std. [4], at a sampling rate of 500 kHz and with a maximum amplitude of 10 V.

2) *CompactRIO-9039:* These test signals are then fed into a commercial CompactRIO-9039 (cRIO-9039) embedded control and acquisition system from NI [42], where the TD-IpDFT algorithm is implemented. The cRIO-9039 combines a reconfigurable Xilinx Kintex-7 325T FPGA with a 1.91-GHz quad-core Intel Atom E3845 real-time

processor. The device is also equipped with two additional modules, the NI-9467 for time synchronization and the NI-9215 for data acquisition. The latter is a four-input channel 16-bit successive approximation register analog-to-digital converter with a maximum conversion rate of 100 kHz and support for signal magnitudes up to 10 V [43].

The deployment of the algorithm is done by allocating the mSDFT, windowing, and TD-QSG functions within the FPGA and programmed in fixed-point arithmetic, while the core functionality is implemented on the real-time processor and kept in the original double precision used in the simulation benchmark. The same mSDFT implementation proposed in [35] is adopted here in combination with the TD-QSG, as shown in Fig. 6. For this, the buffer size D_{f_l} has been increased compared with its theoretical minimum to avoid overwriting issues between the sampling and TD-QSG processes, which operate at different rates. The SE is finalized in the real-time processor together with the assignation of the proper time stamp. Data transfers between the FPGA and the real-time processor are handled by dedicated direct memory access (DMA). The correlation of the processes implemented at the FPGA and real-time processor level with Algorithm 2 is indicated in Fig. 11.

The resulting estimates are then written to a TDMS file and sent to a dedicated computer for post-processing. These are compared with the corresponding reference parameters calculated at the same instant indicated by the time stamps and used to determine the estimation errors. The calculation of the reference parameters is based on the reconstruction of the synthesized test signal whose parameterization for each test is also shared with the host PC. This calculation also accounts for the magnitude distortion and delay introduced by both the calibrator and CompactRIO modules. Time synchronization with UTC time for both the PMU calibrator and the CompactRIO–9039 is achieved by GPS using a stationary unit with an uncertainty 3σ of ± 100 ns through a splitter [44].

B. Validation Tests

A total of 13 tests are performed to validate the theoretical findings obtained using the simulated benchmark. Each validation test is carried out considering a duration of just below 10 s and based on the setup of Fig. 11 and according to the parameterization of Table II. The subsequent testbed has been considered.

1) *Signal Frequency Range Tests:* Three tests corresponding to fundamental frequencies, respectively, equal to 50, 45, and 55 Hz are conducted. These represent the nominal base case, as well as the lower and upper frequency offset boundaries considered in Section V.

2) *Harmonic Distortion Tests:* Three cases are evaluated for a fundamental tone at nominal frequency corrupted by a single 10% interference corresponding to the second, third, or fourth harmonic, respectively. These are the closest harmonics to the fundamental, and thus, those that can result in the greatest impact.

3) *Out-of-Band Interference Tests:* Interference levels equal to 10% and 4% are evaluated for signals characterized

by a fundamental and an interference frequency equal to 47.5 and 25 Hz and 52.5 and 75 Hz, respectively. These pairs were considered since they returned the highest errors under 60 dB in the analysis presented in Section V.

4) *Bandwidth Modulation Tests:* AM and PM are assessed, respectively, by means of a single-test covering the most demanding cases shown in Section V, i.e., a modulating frequency of 5 Hz for amplitudes of 10% (AM) and $\pi/18$ (PM).

5) *Frequency Ramp Test:* A single test is performed for a positive ramp rate of 1 Hz/s. Again, the selection is justified since, as shown in Section V, the ± 1 Hz/s ramps constitute the most challenging cases.

The experimental results are presented for coherence together with those of the simulated benchmark in Section V. The worst case results are presented by means of black circles within Figs. 7–9 and tabulated in Tables III and IV. A very good agreement is shown with their respective simulated cases allowing to demonstrate the consistency of the algorithm's performance.

VII. COMPARISON WITH SoTA IpDFT

This section is intended to discuss the results obtained with the TD-IpDFT compared with other IpDFT-based SE methods in the existing literature, namely, the i-IpDFT [29] and the HT-IpDFT [30], since all these SE methods have been designed to meet the accuracy requirements for the P and M performance classes.

Focusing on the OOBI, which is the most computationally demanding test, the HT-IpDFT [30] has been shown to offer a lower computational cost compared with the i-IpDFT [29] due to the cancellation of negative frequency components offered by the adoption of the analytic signal. However, the HT-IpDFT does not meet the combined requirements of classes P and M for HD (1%) and phase step tests in [4]. The TD-IpDFT satisfies all the accuracy requirements for the P and M classes and also offers a reduction in the total computational cost compared with the i-IpDFT [29], [36]. This is because it mitigates the effects of self-interference by using the in-quadrature complex signal for the estimation, while the i-IpDFT, which is based on the e-IpDFT [28], must iteratively compensate for them on each successive iteration.[12] Taking into account the same parameterization for both methods (Table II), that is, the same type and length of the window and the same number of DFT bins, the i-IpDFT requires a total of $799 + 1646Q$ simple operations and $230 + 502Q$ complex operations based on the updated tuning presented in [36], whereas the TD-IpDFT can perform the estimation with just $171 + 1000Q$ and $37 + 307Q$ operations, respectively. This represents a significant decrease compared with the i-IpDFT. Moreover, considering
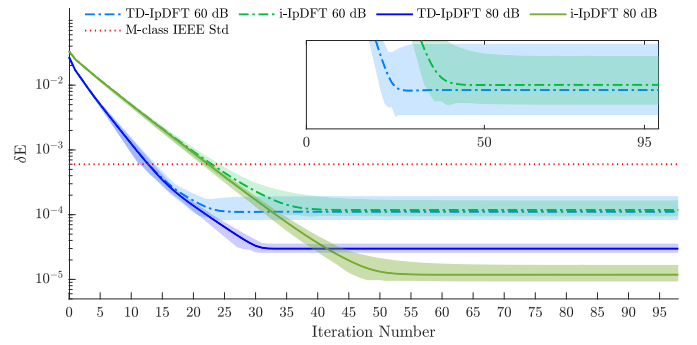

Fig. 12. Performance comparison between TD-IpDFT and i-IpDFT for noise levels with SNR equal to 60 and 80 dB for 200 different runs. δE (19) as a function of the iteration number. Shaded areas are given by the maximum–minimum value pairs, while the solid (80 dB) and dotted-dashed (60 dB) lines represent their mean values across all runs.

the maximum overall error among the entire OOBI range, the TD-IpDFT also shows faster convergence, requiring fewer iterations, for the same maximum error level compared with the i-IpDFT. This is shown in Fig. 12 where a performance comparison between TD-IpDFT and i-IpDFT is presented in terms of δE as a function of the iteration number for noise levels with SNR equal to 60 and 80 dB for 200 different runs. Once again, as with the adjustment of λ_{R_e}, each run evaluates 97 consecutive windows for each interfering tone, and, between runs, the initial phase angle used to generate the reference test signal is shifted by $2\pi/64$. Shaded areas are given by the maximum–minimum value pairs, while the solid (80 dB) and dotted-dashed (60 dB) lines represent their mean values across all runs. It can be seen that the TD-IpDFT requires fewer iterations to achieve the same maximum error level compared with i-IpDFT indistinctly from the noise level, whereas, for the 80-dB noise case, the i-IpDFT can achieve a better global overall accuracy in exchange for a larger number of iterations and higher variability. A higher variability due to noise is observed for the TD-IpDFT under 60 dB as well as a lower overall mean error.

To achieve an equivalent level of performance for both methods and since $Q = 36$ was selected for the TD-IpDFT under a conservative approach as the maximum required to ensure the minimum δE for 60 dB (Section IV-D), the same criteria will be used for the i-IpDFT. Thus, a value of $Q = 44$ is selected for the i-IpDFT. This represents the intersection of the upper boundary of the i-IpDFT shaded area with the maximum value of δE obtained by the TD-IpDFT for $Q = 36$, both under 80-dB noise. Given these, a total decrease of over 50% for simple and complex operations is obtained compared with the i-IpDFT. In return, the TD-IpDFT requires a larger DFT buffer memory to generate the delayed signal. However, it is important to put its size in perspective. According to the values for F_s, K, and T in Table II and considering the MATLAB double numeric data type, the minimum theoretical total buffer memory size required by the TD-IpDFT is just 60 kB. Last, the TD-IpDFT, as opposed to the i-IpDFT, also delivers a complex signal, which allows one to determine its envelope and angle. These could be used to implement identification and correction techniques for the amplitude and phase steps, as done in [45].

---

[12]To draw a meaningful comparison a simplified version of Algorithm 2, aimed at single-tone signals, can be defined consisting of lines 1–4 and 30. This simplified TD-IpDFT can be shown to be more computationally efficient than the e-IpDFT. Taking into account the 3p variant of the e-IpDFT employed in the i-IpDFT and the same parameterization for both methods, the e-IpDFT requires $34K + 47$ simple and $7K + 26$ complex operations, while the simplified TD-IpDFT only requires $12K + 35$ and 20 operations, respectively.

VIII. Conclusion

In this article, an SE technique based on the application of the IpDFT to a delayed in-quadrature complex signal has been presented. The use of the delayed in-quadrature complex signal has been found to be a simple and efficient way to mitigate the detrimental effects caused by the self-interference of the fundamental tone. This allows for a reduction in the total computational complexity of over 50% compared with the i-IpDFT, which relies on an iterative correction based on the e-IpDFT. This is especially significant when the OOBI routine is triggered, since a faster convergence, requiring fewer iterations for the same maximum error level, is obtained. The method represents an alternative to the i-IpDFT and the HT-IpDFT. Like the i-IpDFT, it satisfies all the accuracy requirements defined in the IEC/IEEE Std. 60255-118 while presenting a lower computational cost and it represents an easier and faster implementation than the cascaded Hilbert filter used by the HT-IpDFT. Furthermore, the novel OOBI trigger improves on the one used by the i-IpDFT and by the HT-IpDFT, which only allowed correction of distortions equal to or greater than 10%. The proposed mechanism allows to estimate and removes the effects of those equal to or greater than 4% within the OOBI range. However, in the presence of an interfering tone with an amplitude of less than 4% the same level of accuracy cannot be guaranteed, as the iterative process is not activated. The validity of the metrological assessment conducted using an extensive simulation benchmark has been verified by means of experimental tests through calibration equipment.

Acknowledgment

References

[1] J. De La Ree, V. Centeno, J. S. Thorp, and A. G. Phadke, "Synchronized phasor measurement applications in power systems," *IEEE Trans. Smart Grid*, vol. 1, no. 1, pp. 20–27, Jun. 2010, doi: 10.1109/TSG.2010.2044815.

[2] K. Martin, "Synchrophasors point the way: The emergence of a new technology," *IEEE Electrific. Mag.*, vol. 9, no. 1, pp. 10–24, Mar. 2021, doi: 10.1109/MELE.2020.3047163.

[3] U. Annakage et al., "Application of phasor measurement units for monitoring power system dynamic performance," CIGRE, Paris, France, Tech. Rep., TB 702, pp. 1–137, 2017.

[4] *IEEE/IEC International Standard—Measuring Relays and Protection Equipment—Part 118-1: Synchrophasor for Power Systems—Measurements*, IEC/IEEE Standard 60255-118-1:2018, Dec. 2018, pp. 1–78, doi: 10.1109/IEEESTD.2018.8577045.

[5] A. G. Phadke and J. S. Thorp, *Synchronized Phasor Measurements and Their Applications* (Power Electronics and Power Systems), 2nd ed. Cham, Switzerland: Springer, 2017, p. XIII and 285, doi: 10.1007/978-3-319-50584-8.

[6] J. Ren and M. Kezunovic, "Real-time power system frequency and phasors estimation using recursive wavelet transform," *IEEE Trans. Power Del.*, vol. 26, no. 3, pp. 1392–1402, Jul. 2011, doi: 10.1109/TPWRD.2011.2135385.

[7] J. A. de la O Serna, "Synchrophasor estimation using Prony's method," *IEEE Trans. Instrum. Meas.*, vol. 62, 2013, doi: 10.1109/TIM.2013.2265436.

[8] J. A. de la O Serna, "Dynamic phasor estimates for power system oscillations," *IEEE Trans. Instrum. Meas.*, vol. 56, no. 5, pp. 1648–1657, Oct. 2007, doi: 10.1109/TIM.2007.904546.

[9] M. A. P. Platas-Garza and J. A. de la O Serna, "Dynamic phasor and frequency estimates through maximally flat differentiators," *IEEE Trans. Instrum. Meas.*, vol. 59, no. 7, pp. 1803–1811, Jul. 2010, doi: 10.1109/TIM.2009.2030921.

[10] P. Castello, J. Liu, C. Muscas, P. A. Pegoraro, F. Ponci, and A. Monti, "A fast and accurate PMU algorithm for P+M class measurement of synchrophasor and frequency," *IEEE Trans. Instrum. Meas.*, vol. 63, no. 12, pp. 2837–2845, Dec. 2014, doi: 10.1109/TIM.2014.2323137.

[11] D. Belega, D. Fontanelli, and D. Petri, "Dynamic phasor and frequency measurements by an improved Taylor weighted least squares algorithm," *IEEE Trans. Instrum. Meas.*, vol. 64, no. 8, pp. 2165–2178, Aug. 2015, doi: 10.1109/TIM.2014.2385171.

[12] M. Bertocco, G. Frigo, C. Narduzzi, C. Muscas, and P. A. Pegoraro, "Compressive sensing of a Taylor–Fourier multifrequency model for synchrophasor estimation," *IEEE Trans. Instrum. Meas.*, vol. 64, no. 12, pp. 3274–3283, Dec. 2015, doi: 10.1109/TIM.2015.2450295.

[13] A. T. Munoz and J. A. de la O Serna, "Shanks' method for dynamic phasor estimation," *IEEE Trans. Instrum. Meas.*, vol. 57, no. 4, pp. 813–819, Apr. 2008, doi: 10.1109/tim.2007.913824.

[14] J. A. de la O. Serna and J. Rodríguez-Maldonado, "Instantaneous oscillating phasor estimates with Taylor^k–Kalman filters," *IEEE Trans. Power Syst.*, vol. 26, no. 4, pp. 2336–2344, Nov. 2011, doi: 10.1109/TPWRS.2011.2157539.

[15] J. Liu, F. Ni, J. Tang, F. Ponci, and A. Monti, "A modified Taylor–Kalman filter for instantaneous dynamic phasor estimation," in *Proc. 3rd IEEE PES Innov. Smart Grid Technol. Eur. (ISGT Europe)*, Berlin, Germany, 2012, pp. 1–7, doi: 10.1109/ISGTEurope.2012.6465846.

[16] J. A. de la O Serna and J. Rodríguez-Maldonado, "Taylor–Kalman–Fourier filters for instantaneous oscillating phasor and harmonic estimates," *IEEE Trans. Instrum. Meas.*, vol. 61, no. 4, pp. 941–951, Apr. 2012, doi: 10.1109/TIM.2011.2178677.

[17] Z. D. Drummond, K. E. Claytor, D. R. Allee, and D. M. Hull, "An optimized subspace-based approach to synchrophasor estimation," *IEEE Trans. Instrum. Meas.*, vol. 70, pp. 1–13, 2021, doi: 10.1109/TIM.2020.3017059.

[18] K. Duda and T. P. Zielinski, "P class and M class compliant PMU based on discrete-time frequency-gain transducer," *IEEE Trans. Power Del.*, vol. 37, no. 2, pp. 1058–1067, Apr. 2022, doi: 10.1109/TPWRD.2021.3076831.

[19] J. R. Razo-Hernandez, A. Mejia-Barron, D. Granados-Lieberman, M. Valtierra-Rodriguez, and J. F. Gomez-Aguilar, "A new phasor estimator for PMU applications: P class and M class," *J. Mod. Power Syst. Clean Energy*, vol. 8, no. 1, pp. 55–66, Jan. 2020, doi: 10.35833/MPCE.2018.000584.

[20] A. J. Roscoe, I. F. Abdulhadi, and G. M. Burt, "P and M class phasor measurement unit algorithms using adaptive cascaded filters," *IEEE Trans. Power Del.*, vol. 28, no. 3, pp. 1447–1459, Jul. 2013, doi: 10.1109/TPWRD.2013.2238256.

[21] A. J. Roscoe, "Exploring the relative performance of frequency-tracking and fixed-filter phasor measurement unit algorithms under C37.118 test procedures, the effects of interharmonics, and initial attempts at merging P-class response with M-class filtering," *IEEE Trans. Instrum. Meas.*, vol. 62, no. 8, pp. 2140–2153, Aug. 2013, doi: 10.1109/TIM.2013.2265431.

[22] I. Kamwa, S. R. Samantaray, and G. Joos, "Wide frequency range adaptive phasor and frequency PMU algorithms," *IEEE Trans. Smart Grid*, vol. 5, no. 2, pp. 569–579, Mar. 2014, doi: 10.1109/TSG.2013.2264536.

[23] D. Belega, D. Petri, and D. Dallet, "Frequency estimation of a sinusoidal signal via a three-point interpolated DFT method with high image component interference rejection capability," *Digit. Signal Process.*, vol. 24, pp. 162–169, Jan. 2014, doi: 10.1016/j.dsp.2013.09.014.

[24] I. S. Reljin, B. D. Reljin, and V. D. Papic, "Extremely flat-top windows for harmonic analysis," *IEEE Trans. Instrum. Meas.*, vol. 56, no. 3, pp. 1025–1041, Jun. 2007, doi: 10.1109/TIM.2007.894889.

[25] F. J. Harris, "On the use of windows for harmonic analysis with the discrete Fourier transform," *Proc. IEEE*, vol. 66, no. 1, pp. 51–83, Mar. 1978, doi: 10.1109/PROC.1978.10837.

[26] V. K. Jain, W. L. Collins, and D. C. Davis, "High-accuracy analog measurements via interpolated FFT," *IEEE Trans. Instrum. Meas.*, vol. IM-28, no. 2, pp. 113–122, Mar. 1979, doi: 10.1109/TIM.1979.4314779.

[27] T. Grandke, "Interpolation algorithms for discrete Fourier transforms of weighted signals," *IEEE Trans. Instrum. Meas.*, vol. IM-32, no. 2, pp. 350–355, Jun. 1983, doi: 10.1109/TIM.1983.4315077.

[28] P. Romano and M. Paolone, "Enhanced interpolated-DFT for synchrophasor estimation in FPGAs: Theory, implementation, and validation of a PMU prototype," *IEEE Trans. Instrum. Meas.*, vol. 63, no. 12, pp. 2824–2836, Dec. 2014, doi: 10.1109/TIM.2014.2321463.

[29] A. Derviškadić, P. Romano, and M. Paolone, "Iterative-interpolated DFT for synchrophasor estimation: A single algorithm for P- and M-class compliant PMUs," *IEEE Trans. Instrum. Meas.*, vol. 67, no. 3, pp. 547–558, Mar. 2018, doi: 10.1109/TIM.2017.2779378.

[30] G. Frigo, A. Derviškadić, and M. Paolone, "Reduced leakage synchrophasor estimation: Hilbert transform plus interpolated DFT," *IEEE Trans. Instrum. Meas.*, vol. 68, no. 10, pp. 3468–3483, Oct. 2019, doi: 10.1109/TIM.2018.2879070.

[31] D. Agrez, "Weighted multipoint interpolated DFT to improve amplitude estimation of multifrequency signal," *IEEE Trans. Instrum. Meas.*, vol. 51, no. 2, pp. 287–292, Apr. 2002, doi: 10.1109/19.997826.

[32] L. Zhan, Y. Liu, and Y. Liu, "A Clarke transformation-based DFT phasor and frequency algorithm for wide frequency range," *IEEE Trans. Smart Grid*, vol. 9, no. 1, pp. 67–77, Jan. 2018, doi: 10.1109/TSG.2016.2544947.

[33] D. Belega and D. Petri, "Sine-wave parameter estimation by interpolated DFT method based on new cosine windows with high interference rejection capability," *Digit. Signal Process.*, vol. 33, pp. 60–70, Oct. 2014, doi: 10.1016/j.dsp.2014.07.003.

[34] D. Belega and D. Petri, "Fast procedures for accurate parameter estimation of sine-waves affected by noise and harmonic distortion," *Digit. Signal Process.*, vol. 114, Jul. 2021, Art. no. 103035, doi: 10.1016/j.dsp.2021.103035.

[35] P. Romano and M. Paolone, "An enhanced interpolated-modulated sliding DFT for high reporting rate PMUs," in *Proc. IEEE Int. Workshop Appl. Meas. Power Syst. Proc. (AMPS)*, Sep. 2014, pp. 1–6, doi: 10.1109/AMPS.2014.6947708.

[36] A. Derviškadić and M. Paolone, "Design and experimental validation of an FPGA-based PMU simultaneously compliant with P and M performance classes," *Electr. Power Syst. Res.*, vol. 189, Dec. 2020, Art. no. 106650, doi: 10.1016/j.epsr.2020.106650.

[37] S. Golestan, J. M. Guerrero, and J. C. Vasquez, "Single-phase PLLs: A review of recent advances," *IEEE Trans. Power Electron.*, vol. 32, no. 12, pp. 9013–9030, Dec. 2017, doi: 10.1109/TPEL.2017.2653861.

[38] R. Roy and T. Kailath, "ESPRIT-estimation of signal parameters via rotational invariance techniques," *IEEE Trans. Acoust., Speech, Signal Process.*, vol. 37, no. 7, pp. 984–995, Jul. 1989, doi: 10.1109/29.32276.

[39] K. Duda, "Accurate, guaranteed stable, sliding discrete Fourier transform [DSP tips & tricks]," *IEEE Signal Process. Mag.*, vol. 27, no. 6, pp. 124–127, Nov. 2010, doi: 10.1109/MSP.2010.938088.

[40] G. Frigo, A. Derviškadić, D. Colangelo, J. P. Braun, and M. Paolone, "Characterization of uncertainty contributions in a high-accuracy PMU validation system," *Measurement*, vol. 146, pp. 72–86, Nov. 2019.

[41] National Instruments. (Sep. 21, 2023). *NI PXI-1042Q Chassis.* [Online]. Available: https://www.ni.com/docs/en-U.S./bundle/pxi-1042-1042q-seri/resource/371088a.pdf

[42] National Instruments. (Sep. 21, 2023). *CompactRIO cRIO-9039 Specifications.* [Online]. Available: https://www.ni.com/docs/en-U.S./bundle/crio-9039-specs/page/specs.html

[43] National Instruments. (Sep. 21, 2023). *NI 9215 C Series Voltage Input Module.* [Online]. Available: https://www.ni.com/docs/en-U.S./bundle/ni-9215-specs/page/specs.html

[44] GPS Networking. (Sep. 21, 2023). *DRMALDCBS2X32 Dual Antenna Rack Mount Amplified 2X32 GPS Splitter.* [Online]. Available: https://www.gpsnetworking.com/system/datasheets/148/original/DRMALDCBS2X32-2018.pdf?1610392915

[45] A. Karpilow, M. Paolone, A. Derviškadić, and G. Frigo, "Step change detection for improved ROCOF evaluation of power system waveforms," in *Proc. Int. Conf. Smart Grid Synchronized Meas. Anal. (SGSMA)*, Split, Croatia, 2022, pp. 1–7, doi: 10.1109/SGSMA51733.2022.9806005.

César García-Veloso (Graduate Student Member, IEEE) was born in Galicia, Spain, in 1993. He received the B.Sc. degree in energy engineering from the University of Vigo, Galicia, Spain, in 2015, and the M.Sc. degree in smart electrical networks and systems from the KTH Royal Institute of Technology, Stockholm, Sweden, and the Technical University of Catalonia, Barcelona, Spain, in 2017. He is currently pursuing the Ph.D. degree with the Department of Electrical Engineering, University of Seville, Seville, Spain, with a focus on frequency measurement and estimation in power systems.

From 2018 to 2020, he was a Technical Consultant with Hitachi ABB Power Grids, Madrid, Spain.

Mr. García-Veloso was a recipient of the Basil Papadias Award for the third Best Student Paper at the 2023 IEEE PowerTech Conference in Belgrade.

Mario Paolone (Fellow, IEEE) received the M.Sc. (Hons.) and Ph.D. degrees in electrical engineering from the University of Bologna, Bologna, Italy, in 1998 and 2002, respectively.

In 2005, he was an Assistant Professor in power systems with the University of Bologna, where he was with the Power Systems Laboratory until 2011. Since 2011, he has been with the Swiss Federal Institute of Technology, Lausanne, Switzerland, where he is currently a Full Professor and the Chair of the Distributed Electrical Systems Laboratory. His most significant contributions are in the field of PMU-based situational awareness of active distribution networks (ADNs), and exact, convex, and computationally efficient methods for the optimal planning and operation of ADNs. His research interests focus on power systems with particular reference to real-time monitoring and operational aspects and power system protections, dynamics, and transients.

Dr. Paolone was the Founding Editor-in-Chief of the Elsevier journal *Sustainable Energy, Grids and Networks*.

José María Maza-Ortega (Member, IEEE) received the M.Sc. and Ph.D. degrees in electrical engineering from the University of Seville, Seville, Spain, in 1996 and 2001, respectively.

Since 1997, he has been with the Department of Electrical Engineering, University of Seville, where he is currently a Full Professor. His research interests include power quality, integration of renewable energies, control of active distribution networks, and power electronics applications to transmission and distribution systems.